

ISOCHRONS IN PRESOLAR GRAPHITE GRAINS FROM ORGUEIL

ERNST ZINNER AND MANAVI JADHAV¹

Laboratory for Space Sciences and the Physics Department, Washington University, One Brookings Drive, St. Louis, MO 63130, USA; ekz@wustl.edu
Received 2012 December 17; accepted 2013 March 16; published 2013 April 18

ABSTRACT

Primitive meteorites contain tiny dust grains that condensed in stellar outflows and explosions. These stardust grains can be extracted from their host meteorites and studied in detail in the laboratory. We investigated depth profiles of the Al–Mg, Ca–K, and Ti–Ca isotopic systems obtained during NanoSIMS isotopic analysis of presolar graphite grains from the CI carbonaceous meteorite Orgueil. Large $^{26}\text{Al}/^{27}\text{Al}$, $^{41}\text{Ca}/^{40}\text{Ca}$, and $^{44}\text{Ti}/^{48}\text{Ti}$ ratios, inferred from ^{26}Mg , ^{41}K , and ^{44}Ca excesses from the decay of the short-lived radioisotopes ^{26}Al , ^{41}Ca , and ^{44}Ti , indicate a supernova (SN) origin. From the depth distribution of the radiogenic isotopes and the stable isotopes of their parent elements we constructed isochron-type correlation plots. The plots indicate quantitative retention of radiogenic ^{26}Mg , ^{41}K , and ^{44}Ca in most grains. Deviations from straight lines in the Al–Mg and Ca–K plots can be explained by contamination with ^{27}Al and isotopically normal Ca, respectively. For the Ti–Ca system in some grains, the lack of parent–daughter correlation indicates either redistribution of radiogenic ^{44}Ca or heterogeneity in the initial $^{44}\text{Ti}/^{48}\text{Ti}$ ratio. We also obtained Si isotopic depth profiles in three graphite grains with large ^{29}Si and ^{30}Si excesses, for which a SN origin has been proposed. In two grains no Si-rich subgrains are observed; in the third grain with an apparent Si-rich subgrain the anomalous Si isotopic ratios in the subgrain are the same as in the rest of the graphite host. Our studies show that by measuring depth profiles, information on presolar grains can be obtained that cannot be obtained by whole-grain analysis.

Key words: dust, extinction – nuclear reactions, nucleosynthesis, abundances – stars: abundances – supernovae: general

1. INTRODUCTION

Primitive meteorites contain stardust, tiny dust grains that condensed in the outflows of late-type stars and in supernova (SN) ejecta (Clayton & Nittler 2004; Lodders & Amari 2005; Lugaro 2005; Zinner 2007). Their detailed study in the laboratory provides information on stellar nucleosynthesis, physical and chemical conditions in stellar atmospheres, the chemical evolution of the galaxy, and conditions in the early solar system. Graphite grains (Amari et al. 1990) are one of the many types of presolar grains identified to date (e.g., Zinner 2007). Although more silicon carbide (SiC) grains than graphite grains have been studied, more than a thousand graphite grains have been analyzed for their isotopic compositions (Hynes & Gyngard 2009). Almost all of these data have been obtained on graphite grains from two separation series, one from the CM2 Murchison meteorite, the K-series (Amari et al. 1994), and the other one from the CI1 Orgueil meteorite (Jadhav et al. 2006). In both cases, different densities have been available for study and it has been found that grains of different densities originate from different stellar sources (Zinner 2007): low-density (LD) grains from Type II SNe (Amari et al. 1995, 1996; Nittler et al. 1996; Travaglio et al. 1999; Stadermann et al. 2005; Zinner et al. 2006) and high-density (HD) grains mostly from asymptotic giant branch (AGB) stars of low metallicity, although grains with a SN origin are also found among them (Croat et al. 2005; Jadhav et al. 2006, 2008, 2013; Zinner et al. 2006). In addition, some HD grains have extreme Ca and Ti isotopic anomalies and it has been proposed that they originate from born-again AGB stars (Jadhav et al. 2008). In this paper, we follow the tradition of calling carbonaceous presolar grains that are neither diamond nor SiC graphite (Amari et al. 1990, 1995; Hoppe et al. 1995). However, as Wopenka et al. (2013) have discussed

in detail, transmission electron microscope (Bernatowicz et al. 1991, 1996; Croat et al. 2003, 2008) and Raman microprobe analyses (Wopenka et al. 2011a, 2011b, 2013) have shown that not all grains consisting of sp^2 -bonded carbon are well crystallized graphite and many have structures ranging from poorly crystallized to amorphous.

Generally, isotopic measurements on individual grains by Secondary Ion Mass Spectrometry (SIMS) in the ion microprobe or by Resonance Ion Mass Spectrometry (RIMS) have not tried to determine internal distributions in the grains' elemental or isotopic compositions. An exception are NanoSIMS studies that involved isotopic imaging, either on whole grains (Zinner et al. 2010b; Groopman et al. 2012) or on ultrathin slices of grains (Stadermann et al. 2005; Groopman et al. 2012). However, some information on the internal distribution of elements and isotopes in presolar grains exists in the form of depth profiles obtained during isotopic measurements in the NanoSIMS. During such measurements, the primary ion beam is rastered over an area covering the whole grains. Analyses involve many cycles, and as the primary ion beam removes sample material layer by layer, the depth of material sputtered away is proportional to the time of analysis. In this way, we can construct elemental and isotopic depth profiles. This has been done by Marhas et al. (2008) during Fe and Ni isotopic analysis of presolar SiC grains. These authors found Fe-rich subgrains, especially in type X SiC grains from SNe. In a similar way, Lin et al. (2010) reported depth profiles of Al and Mg in SiC X grains and investigated possible heterogeneity of the initial $^{26}\text{Al}/^{27}\text{Al}$ ratio in these grains.

In the present paper, we investigate what type of information can be obtained from depth profiles in graphite grains from the Orgueil carbonaceous chondrite.

2. SAMPLES AND EXPERIMENTAL PROCEDURES

The data for this study were obtained on graphite grains from the LD fraction OR1d (1.75–1.92 g cm⁻³) and HD fraction OR1f

¹ Current address: Hawaii Institute of Geophysics and Planetology, University of Hawaii at Manoa, 1680 East-West Road, Post 602, Honolulu, HI 96822, USA.

(2.02–2.04 g cm⁻³). Most of the bulk data (i.e., averages of isotopic measurements on whole grains, but not depth profiles) have been published previously (Jadhav et al. 2006, 2008, 2013). In addition, we present data from an unpublished study of graphite grain mount OR1f3m (3m denotes the third grain mount of a given fraction; see Jadhav et al. 2013 for an explanation of grain mount nomenclature).

The typical sequence of isotopic analyses in the NanoSIMS was to first measure C, N, O, and Si as negative secondary ions produced with a primary Cs⁺ beam, and subsequently Mg, Al, K, Ca, and Ti as positive secondary ions produced with an O⁻ beam. Negative secondary ions were measured in different combinations: C and Si, followed by O (¹⁶O and ¹⁸O only) and N (measured as CN); C and O, followed by O and Si; C and N, followed by O and Si. These measurements were made in multidetection and so were the following Al–Mg measurements. These measurements were followed by measurements of K (³⁹K and ⁴¹K), Ca (⁴⁰Ca, ⁴²Ca, ⁴³Ca, and ⁴⁴Ca) and ⁴⁸Ti (sometimes also ⁴⁷Ti) made in combined mode (multidetection and magnetic peak jumping), and finally by measurements of ⁴⁰Ca and Ti (all five stable isotopes), also made in combined mode. During the last set of measurements, we also measured ⁵¹V and ⁵²Cr in order to make corrections for ⁵⁰V and ⁵⁰Cr interferences (for further measurement details, see Jadhav et al. 2013). This sequence of analyses means that different layers were measured during different sets of measurements and, consequently, that depth profiles were obtained from different depths of the grains. We do not have exact information on the depths of different depth profiles but, from SEM images of the grains obtained before and after NanoSIMS analysis, estimate that the depth analyzed in each profile is ~0.5–1 μm.

Because different elements have different ion yields, determination of the ratios ²⁷Al/²⁴Mg, ⁴⁰Ca/³⁹K, and ⁴⁸Ti/⁴⁰Ca from the ion ratios requires a correction in the form of a sensitivity factor. This factor SF is defined as $^{27}\text{Al}/^{24}\text{Mg} = \text{SF} \times ^{27}\text{Al}^+ / ^{24}\text{Mg}^+$ and likewise for the other ratios. For Al/Mg we used as SF of 0.525, for Ca/K 3.0, and for Ti/Ca 2.83.

3. RESULTS AND DISCUSSION

The bulk isotopic data of the grains for which we report depth profiles are given in Table 1 in the sequence of the profiles shown. We report four types of depth profiles: (1) Al–Mg profiles of grains that show evidence for the initial presence of short-lived ²⁶Al ($T_{1/2} = 7.17 \times 10^5$ yr). For these grains we also plot “isochron” correlation plots of $\delta^{26}\text{Mg}/^{24}\text{Mg}^2$ values versus ²⁷Al/²⁴Mg ratios. We put isochron in quotation marks because, as discussed in more detail below, these plots are not true isochron plots that can be used to determine a formation time by radiometric dating. (2) Ca–K profiles of grains that show the initial presence of ⁴¹Ca ($T_{1/2} = 1.05 \times 10^5$ yr) and corresponding “isochron” plots. (3) Ti–Ca profiles of grains that show the initial presence of ⁴⁴Ti ($T_{1/2} = 60$ yr) and corresponding “isochron” plots. (4) Si profiles of grains that show large ^{29,30}Si excesses. In order to reduce scatter of the profiles and “isochron” plots we plot a running average of from 3 to 10 cycles for the isotopic profiles and use the sums of 5 and 10 cycles, respectively, for calculating the ratios for the “isochron” plots. The errors plotted in the “isochron” plots are 1σ errors calculated from the total counts in the ranges of cycles.

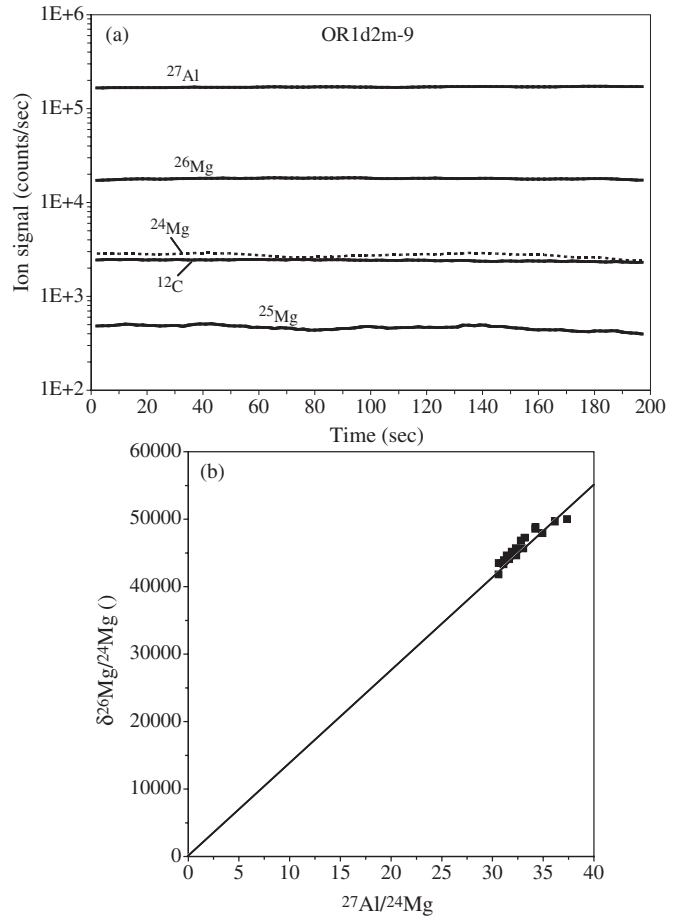


Figure 1. (a) Secondary ion signals as a function of time during isotopic analysis of LD grain OR1d2m-9 from the Orgueil carbonaceous chondrite. As material is sputtered away during analysis, the time profile corresponds to a depth profile in the grain. (b) Isochrone correlation plot of $\delta^{26}\text{Mg}/^{24}\text{Mg}$ versus ²⁷Al/²⁴Mg obtained from averages of five cycles during Al–Mg isotopic analysis shown in panel (a). In this and all other “isochron” plots, isotopic ratios of Mg, K, and Ca are plotted in delta values, and deviations from the normal ratio in permil. The errors in this and all other plots are 1σ errors based on counting statistics.

3.1. Al–Mg System

3.1.1. Grain OR1d2m-9

Figure 1 shows a depth profile plot of ¹²C, ²⁷Al, and the three Mg isotopes and a plot of $\delta^{26}\text{Mg}/^{24}\text{Mg}$ versus ²⁷Al/²⁴Mg for the LD grain OR1d2m-9. The N, O, and Si isotopic ratios of this grain (Table 1) indicated that it has a SN origin. We note that Figure 1(a) shows the raw ion signals. Because the positive ion yield of C is very low compared to that of Mg and Al (Hinton 1990), the ²⁷Al and ²⁶Mg ion signals are much larger than that of ¹²C, in spite of the fact that carbon is the major element of the grain. In contrast to the profile plot in Figure 1(a), for the “isochron” plot in Figure 1(b) we applied a sensitivity factor between Mg and Al determined from analysis of a spinel standard so that the ²⁷Al/²⁴Mg ratio is the true ratio and not the ion ratio. This is also done for all subsequent “isochron” plots. As can be seen from Figure 1(a), the ²⁶Mg signal is much higher than the ²⁴Mg signal, resulting in very large $\delta^{26}\text{Mg}/^{24}\text{Mg}$ values in Figure 1(b). The ²⁷Al and ²⁶Mg signals are essentially constant throughout the profile, indicating a constant initial ²⁶Al/²⁷Al ratio in the grain. There is some variation in the ²⁴Mg signal, giving rise to a limited range in $\delta^{26}\text{Mg}/^{24}\text{Mg}$ and ²⁷Al/²⁴Mg (Figure 1(b)). However, $\delta^{26}\text{Mg}/^{24}\text{Mg}$ and

² δ-values are deviations in permil (‰) from standard ratios; e.g., $\delta^i\text{Mg}/^{24}\text{Mg} = 1000 \times \{(^i\text{Mg}/^{24}\text{Mg})_{\text{sample}} / (^i\text{Mg}/^{24}\text{Mg})_{\text{standard}} - 1\}$.

Table 1
Isotopic Ratios of Orgueuil Graphite Grains

Grain Label	Type ^a	Size (μm)	$^{12}\text{C}/^{13}\text{C}$	$^{14}\text{N}/^{15}\text{N}$	$^{16}\text{O}/^{18}\text{O}$	$\delta^{29}\text{Si}/^{28}\text{Si}$ (‰)	$\delta^{30}\text{Si}/^{28}\text{Si}$ (‰)				
(A) Al–Mg system											
OR1d2m-9	LD	3.6	118.9 ± 1.7	203.4 ± 1.9	68.0 ± 0.7	-295 ± 5	-457 ± 4				
OR1d2m-18	LD	5.5	76.5 ± 1.1	239.2 ± 2.1	378.7 ± 4.2	-37 ± 6	-52 ± 7				
OR1d2m-19	LD	4	39.1 ± 0.5	116.7 ± 1.1	59.2 ± 0.6	-85 ± 6	-110 ± 7				
OR1d3m-27	LD	3.0	95.8 ± 0.6	214.3 ± 1.3	328.2 ± 5.4	-4 ± 12	-76 ± 14				
OR1d4m-16	LD	3.5	103.9 ± 1.0	182.6 ± 1.4	113.1 ± 1.2	-59 ± 9	-27 ± 12				
OR1d4m-20	LD	2	27.2 ± 0.3	165.5 ± 2.4	29.8 ± 0.3	-230 ± 13	-341 ± 15				
(B) Ca–K system											
OR1f3m-9	HD	7	362.5 ± 2.6	276.9 ± 1.7	557.7 ± 13.9	-30 ± 11	-31 ± 13				
OR1f2m-o68	HD	15	245.1 ± 2.5	87.0 ± 1.3	511.8 ± 9.6	1341 ± 35	896 ± 33				
(C) Ti–Ca system											
OR1f2m-1	HD	3	14.2 ± 0.1	266.9 ± 18.0	519.5 ± 7.3	-20 ± 13	-35 ± 18				
OR1f2m-25	HD	6	743.1 ± 2.2	463.9 ± 13.0	530.9 ± 10.5	-30 ± 19	-90 ± 23				
OR1f2m-o67	HD	12	3.9 ± 0.0	50.7 ± 0.8	499.9 ± 11.3	-325 ± 18	235 ± 30				
OR1f3m-25	HD	5	485.9 ± 3.5	280.9 ± 3.1	552.6 ± 15.1	-55 ± 16	-30 ± 20				
OR1d4m-9	LD	5	110.6 ± 1.1	259.3 ± 2.5	444.4 ± 6.4	-111 ± 11	-132 ± 15				
OR1f3m-12	HD	10	91.6 ± 0.7	273.9 ± 1.9	542.4 ± 13.8	-57 ± 13	15 ± 16				
(D) Si isotopes											
OR1f2m-o68	HD	15	245.1 ± 2.5	87.0 ± 1.3	511.8 ± 9.6	1341 ± 35	896 ± 33				
OR1f1m-70	HD	4	158.4 ± 1.6	149.5 ± 2.4	505.9 ± 17.6	1043 ± 34	916 ± 36				
OR1f1m-16	HD	7	77.4 ± 0.8	291.2 ± 7.3	523.0 ± 21.8	177 ± 13	583 ± 16				
Grain Label	$\delta^{25}\text{Mg}/^{24}\text{Mg}$ (‰)	$\delta^{25}\text{Mg}/^{24}\text{Mg}^b$ (‰)	$\delta^{26}\text{Mg}/^{24}\text{Mg}$ (‰)	$\delta^{26}\text{Mg}/^{24}\text{Mg}^b$ (‰)	$^{26}\text{Al}/^{27}\text{Al}$	$^{26}\text{Al}/^{27}\text{Al}^c$	$\delta^{41}\text{K}/^{39}\text{K}$ (‰)	$\delta^{41}\text{K}/^{39}\text{K}^b$ (‰)	$^{41}\text{Ca}/^{40}\text{Ca}$ (10^{-4})	$^{41}\text{Ca}/^{40}\text{Ca}^c$ (10^{-4})	
(A) Al–Mg system											
OR1d2m-9	366 ± 10	437	45637 ± 169	51000	0.1980 ± 0.0008	0.198					
OR1d2m-18	757 ± 21	1260	59800 ± 479	142000	0.1460 ± 0.0007	0.154					
OR1d2m-19	1247 ± 16	3200	130001 ± 458	448000	0.3080 ± 0.0011	$0.28\text{--}0.35?$					
OR1d3m-27	391 ± 7	800	7649 ± 32	14600	0.0350 ± 0.0002	0.051	-21 ± 11				
OR1d4m-16	1 ± 18	~ 0	232309 ± 4273	720000	0.4820 ± 0.0040	0.586	29 ± 45				
OR1d4m-20	1824 ± 46	~ 2500	3233134 ± 28488	4400000	0.6990 ± 0.0061	0.736	66 ± 79				
(B) Ca–K system											
OR1f3m-9	-22 ± 12		-17 ± 7				1917 ± 272	3500	38.9 ± 3.7	40.7	
OR1f2m-o68	-26 ± 7		-25 ± 7				19949 ± 99	40000	102.8 ± 5.6	106.3	
(C) Ti–Ca system											
OR1f2m-1	22 ± 25		-15 ± 23				13 ± 33				
OR1f2m-25	18 ± 15		47 ± 14				307 ± 12		59.8 ± 15.0		
OR1f2m-o67	1 ± 78		1593 ± 140		0.0097 ± 0.0009		12 ± 19				
OR1f3m-25	-56 ± 40		-74 ± 36				-55 ± 45				
OR1d4m-9	-15 ± 16		1779 ± 29		0.0105 ± 0.0002		0 ± 24				
OR1f3m-12	6 ± 12		-4 ± 7				21 ± 32				
Grain Label	$\delta^{42}\text{Ca}/^{40}\text{Ca}$ (‰)	$\delta^{43}\text{Ca}/^{40}\text{Ca}$ (‰)	$\delta^{44}\text{Ca}/^{40}\text{Ca}$ (‰)	$\delta^{44}\text{Ca}/^{40}\text{Ca}^b$ (‰)	$^{44}\text{Ti}/^{48}\text{Ti}$ (10^{-4})	$^{44}\text{Ti}/^{48}\text{Ti}^c$ (10^{-4})					
(A) Al–Mg system											
OR1d2m-9											
OR1d2m-18											
OR1d2m-19											
OR1d3m-27	-2 ± 17	51 ± 27	-11 ± 16								
OR1d4m-16	71 ± 10	202 ± 18	1 ± 4								
OR1d4m-20	103 ± 27	314 ± 65	26 ± 14								
(B) Ca–K system											
OR1f3m-9	49 ± 23	65 ± 44	36 ± 16								
OR1f2m-o68	996 ± 13	2839 ± 41	289 ± 7								
(C) Ti–Ca system											
OR1f2m-1	-152 ± 96	156 ± 239	6018 ± 203	28000	4.42 ± 0.15	4.42					
OR1f2m-25	93 ± 22	90 ± 42	1584 ± 26	4300	23.8 ± 0.4	$17.8\text{--}26.9$					
OR1f2m-o67	63 ± 52	15 ± 107	3767 ± 77	6200	17.7 ± 0.4	17.7					
OR1f3m-25	-69 ± 98	487 ± 263	1193 ± 86	5800	1.45 ± 0.11	$0\text{--}3.0$					
OR1d4m-9	43 ± 26	125 ± 59	1460 ± 22	3800	74.7 ± 1.2	$44\text{--}450$					
OR1f3m-12	15 ± 25	157 ± 52	377 ± 21	500	231 ± 13	230					
Grain Label	$\delta^{46}\text{Ti}/^{48}\text{Ti}$ (‰)	$\delta^{47}\text{Ti}/^{48}\text{Ti}$ (‰)	$\delta^{49}\text{Ti}/^{48}\text{Ti}$ (‰)	$\delta^{50}\text{Ti}/^{48}\text{Ti}$ (‰)							
(A) Al–Mg system											
OR1d2m-9											
OR1d2m-18											
OR1d2m-19											
OR1d3m-27	35 ± 42	32 ± 30	1326 ± 60								
OR1d4m-16	-57 ± 16	-55 ± 16	587 ± 36								
OR1d4m-20											

Table 1
(Continued)

Grain Label	$\delta^{46}\text{Ti}/^{48}\text{Ti}$ (‰)	$\delta^{47}\text{Ti}/^{48}\text{Ti}$ (‰)	$\delta^{49}\text{Ti}/^{48}\text{Ti}$ (‰)	$\delta^{50}\text{Ti}/^{48}\text{Ti}$ (‰)
(B) Ca–K system				
OR1f3m-9				
OR1f2m-o68	1975 ± 160	327 ± 98	1562 ± 169	2184 ± 329
(C) Ti–Ca system				
OR1f2m-1	-15 ± 8	-28 ± 9	161 ± 11	44 ± 15
OR1f2m-25	58 ± 5	-32 ± 12	754 ± 20	214 ± 23
OR1f2m-o67	2 ± 4	14 ± 4	169 ± 5	236 ± 6
OR1f3m-25	792 ± 35	122 ± 47	1802 ± 78	5300 ± 105
OR1d4m-9	-161 ± 13	-135 ± 13	199 ± 25	±
OR1f3m-12	31 ± 30	50 ± 52	172 ± 39	311 ± 283

Notes.^a LD: low-density grains (1.75–1.92 g cm⁻³); HD: high-density grains (2.02–2.04 g cm⁻³).^b Maximum value in profile.^c Ratio obtained from isochron plot.

$^{27}\text{Al}/^{24}\text{Mg}$ are well correlated and the correlation line goes through the origin of the plot, consistent with a constant $^{26}\text{Al}/^{27}\text{Al}$ ratio. The $^{26}\text{Al}/^{27}\text{Al}$ ratio derived from the slope of this plot is the ratio at the time of grain formation. This ratio is obtained in the following way: if $^{26}\text{Mg}^*$ is radiogenic ^{26}Mg derived from the decay of ^{26}Al , $^{26}\text{Al}/^{27}\text{Al} = ^{26}\text{Mg}^*/^{27}\text{Al}$. However, $\delta^{26}\text{Mg}/^{24}\text{Mg} = 1000 \times \{(^{26}\text{Mg}/^{24}\text{Mg})_{\text{sample}} / (^{26}\text{Mg}/^{24}\text{Mg})_{\text{standard}} - 1\}$. Since $^{26}\text{Mg}_{\text{sample}} = ^{26}\text{Mg}_{\text{intr}} + ^{26}\text{Mg}^*$, where $^{26}\text{Mg}_{\text{intr}}$ is the intrinsic ^{26}Mg of the sample, and if $(^{26}\text{Mg}_{\text{intr}} / ^{24}\text{Mg})_{\text{sample}}$ is close to $(^{26}\text{Mg}/^{24}\text{Mg})_{\text{standard}}$, $\delta^{26}\text{Mg}/^{24}\text{Mg} = 1000 \times (^{26}\text{Mg}^* / ^{24}\text{Mg})_{\text{sample}} / (^{26}\text{Mg}/^{24}\text{Mg})_{\text{standard}}$. It follows that the slope of the line in Figure 1(b), i.e., $(\delta^{26}\text{Mg}/^{24}\text{Mg}) / (^{27}\text{Al}/^{24}\text{Mg})$, is $1000 \times (^{26}\text{Mg}^* / ^{27}\text{Al}) / (^{26}\text{Mg}/^{24}\text{Mg})_{\text{standard}}$ or $^{26}\text{Al}/^{27}\text{Al} = ^{26}\text{Mg}^* / ^{27}\text{Al} = 0.001 \times \text{slope} \times (^{26}\text{Mg}/^{24}\text{Mg})_{\text{standard}}$, and if $(^{26}\text{Mg}/^{24}\text{Mg})_{\text{standard}}$ is the solar ratio of 0.13932, $^{26}\text{Al}/^{27}\text{Al} = 1.393 \times 10^{-4} \times \text{slope}$.

Because the correlation line in Figure 1(b) goes through the origin, the $^{26}\text{Al}/^{27}\text{Al}$ ratio derived from the plot is the same as that obtained from the bulk measurement (Table 1). Since $^{26}\text{Al}/^{27}\text{Al}$ ratios can vary within a given SN and among different SNe, the correlation plot in Figure 1(b) does not provide any temporal information, i.e., it is not a true isochron. For the plot to be an isochron, grains would have to form at different times from a reservoir that at a given original time (time zero) had a uniform $^{26}\text{Al}/^{27}\text{Al}$ ratio. We use the term “isochron” because the correlation plots resemble true isochron plots. The fact that there exists a perfect (within errors) correlation between $\delta^{26}\text{Mg}/^{24}\text{Mg}$ and $^{27}\text{Al}/^{24}\text{Mg}$ indicates that there was no disturbance of the Al–Mg system and that no preferential loss of radiogenic ^{26}Mg has taken place, at least within the analyzed volume. It also indicates that there was no heterogeneity of the $^{26}\text{Al}/^{27}\text{Al}$ ratio within the analyzed volume. The high inferred $^{26}\text{Al}/^{27}\text{Al}$ ratio of 0.2 confirms that the grain has a SN origin (e.g., Travaglio et al. 1999; Rauscher et al. 2002).

3.1.2. Grain OR1d2m-18

Figure 2 shows depth profiles and $\delta^{26}\text{Mg}/^{24}\text{Mg}$ versus $^{27}\text{Al}/^{24}\text{Mg}$ and $\delta^{25}\text{Mg}/^{24}\text{Mg}$ versus $^{27}\text{Al}/^{24}\text{Mg}$ plots of another LD SN grain, OR1d2m-18. In contrast to the previous grain, while the ^{27}Al and ^{26}Mg signals are still fairly well correlated, the ^{24}Mg and ^{25}Mg profiles show large variations (Figure 2(a)), resulting in a large range of $\delta^{26}\text{Mg}/^{24}\text{Mg}$ and the $^{27}\text{Al}/^{24}\text{Mg}$ ratio (Figure 2(b)). Again, there exists an essentially perfect correlation between these two parameters, better than in Figure 1(b), because it extends over a larger range. However,

the correlation line through the data points does not go through the origin but intercepts the x -axis at an $^{27}\text{Al}/^{24}\text{Mg}$ value of 7.9. Adding Al to the original ^{26}Al -containing intrinsic Al would shift data points to the right, but adding a constant amount of Al results in a correlation plot that goes through the origin and has a smaller slope.

In order to investigate the behavior of correlation plots if isotopically normal Mg and/or Al are added, we performed a series of simulations. The details are discussed in the Appendix. The case of grain OR1d2m-18 is apparently similar to that shown in Figures 19(a) and (b) (Case a) in the Appendix. As shown there, contamination with Al whose amount is proportional to the normal Mg results in a correlation line with larger slope and a positive intercept with the x -axis. Inspection of Figure 2(a) shows that the curves for ^{27}Al and ^{26}Mg are not exactly parallel but that there is a relative excess of ^{27}Al on the left side of the depth profile. The $^{27}\text{Al}/^{26}\text{Mg}$ ion ratio varies from 16.5 at the beginning of the profile to 12.4 at the end. However, this latter ratio is already reached after ~ 250 s and if we assume this to be the true intrinsic ratio, we obtain an inferred $^{26}\text{Al}/^{27}\text{Al}$ ratio of 0.154. From the slope of the correlation line we obtain a ratio of 0.164. Figure 2(b) shows also the average $\delta^{26}\text{Mg}/^{24}\text{Mg}$ and $^{27}\text{Al}/^{24}\text{Mg}$ values obtained from the whole grain analysis. If this point is connected to the origin, the inferred $^{26}\text{Al}/^{27}\text{Al}$ ratio is 0.146, the value given in Table 1. This analysis provides several important lessons. The $\delta^{26}\text{Mg}/^{24}\text{Mg}$ value obtained from the whole grain analysis (59,800‰) is only an average and much higher values are reached in the depth profile (Figure 2(b)). The $^{26}\text{Al}/^{27}\text{Al}$ ratio inferred from the average $\delta^{26}\text{Mg}/^{24}\text{Mg}$ and $^{27}\text{Al}/^{24}\text{Mg}$ values is smaller than the true intrinsic ratio, in this case because of the presence of Al contamination. On the other hand, the ratio obtained from the slope of the correlation line is too large, as discussed in the Appendix. If we connect the highest point in Figure 2(b) with the origin, we derive an $^{26}\text{Al}/^{27}\text{Al}$ ratio of 0.154, the same as we obtained from the $^{26}\text{Mg}/^{27}\text{Al}$ ratio in the inner part of the depth profile. It appears that the Mg and Al contamination in this region is so small that they become negligible, and the intrinsic Mg and Al dominate.

This is confirmed by the $\delta^{25}\text{Mg}/^{24}\text{Mg}$ versus $^{27}\text{Al}/^{24}\text{Mg}$ plot shown in Figure 2(c). As can be seen, the $\delta^{25}\text{Mg}/^{24}\text{Mg}$ values at low $^{27}\text{Al}/^{24}\text{Mg}$ ratios, which represent data points at the beginning of the profile that are dominated by contamination with normal Mg, are low. As we move along the depth profile to regions with essentially no Mg contamination, the $\delta^{25}\text{Mg}/^{24}\text{Mg}$ levels off at ~ 1200 ‰, much higher than the average value of

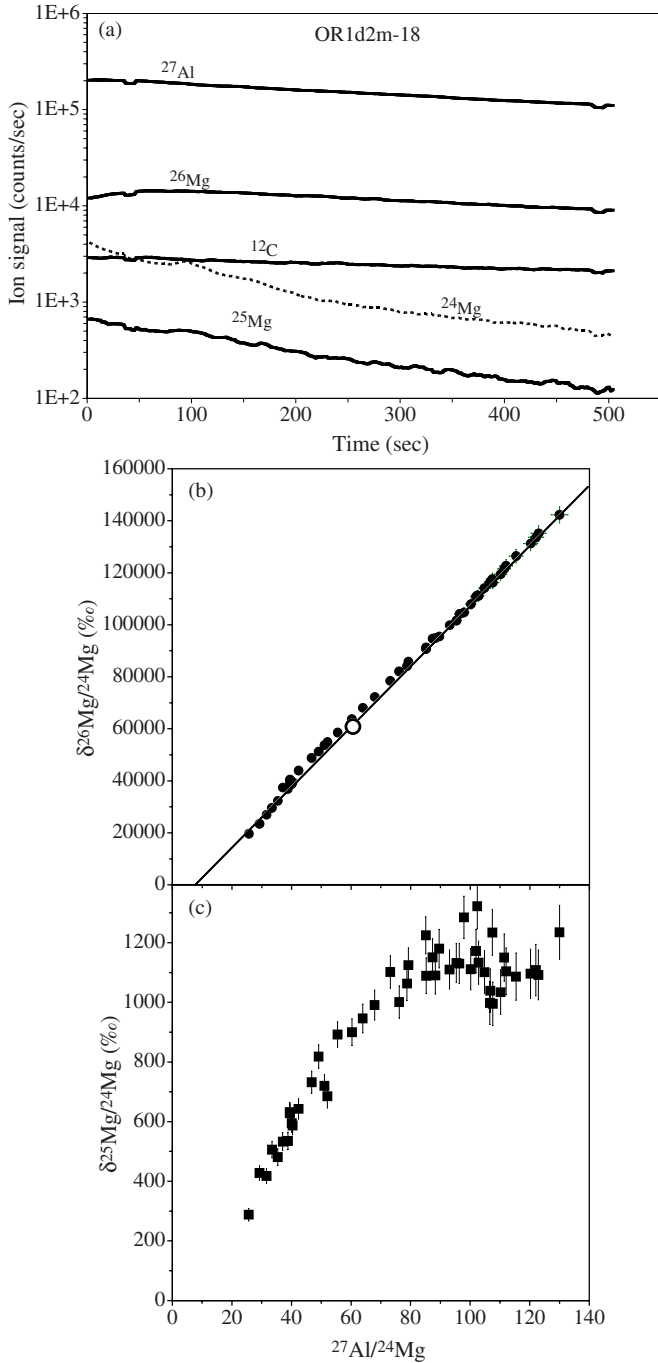


Figure 2. (a) Profiles of secondary ion signals for LD grain OR1d2m-18. (b) Isotope correlation plot obtained from averages of five cycles. The correlation line intercepts the x -axis. The large open circle represents the average ratios measured. (c) Plot of $\delta^{25}\text{Mg}/^{24}\text{Mg}$ vs. $^{27}\text{Al}/^{24}\text{Mg}$. As Mg of normal isotopic composition is sputtered away (panel (a)), the intrinsic ^{25}Mg excess increases.

757‰ (Table 1). It has been pointed out some time ago (e.g., Hoppe et al. 1995) that, because of possible contamination, isotopic anomalies measured in presolar grains have to be considered lower limits. Although even in grain OR1d2m-18 there might still be small amounts of Mg and Al contamination at the end of the depth profile. The analysis based on the depth profile we present here constitutes an important improvement over the information obtained from the average whole grain analysis that is usually reported.

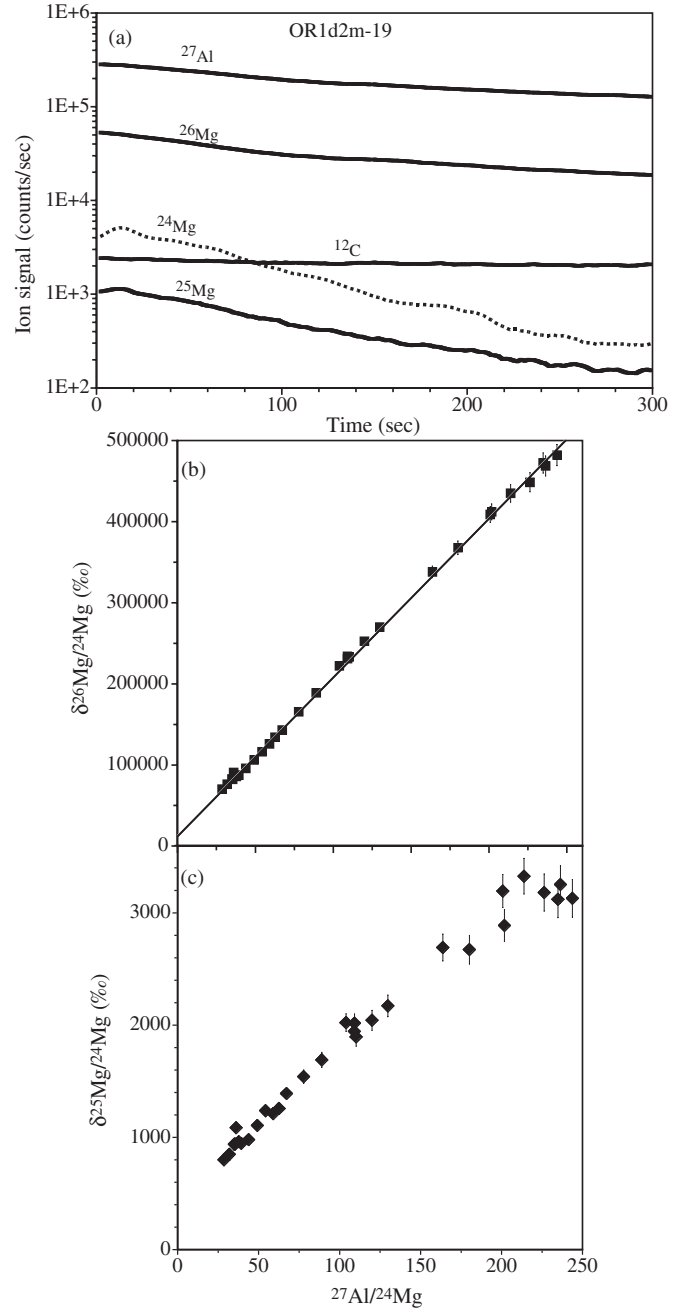


Figure 3. (a) Profiles of secondary ion signals for LD grain OR1d2m-19. (b) Isotope correlation plot obtained from averages of five cycles. The correlation line intercepts the y -axis. (c) Plot of $\delta^{25}\text{Mg}/^{24}\text{Mg}$ vs. $^{27}\text{Al}/^{24}\text{Mg}$.

One important conclusion that can be made for grain OR1d2m-18 with even higher certainty than for grain OR1d2m-9 is that $^{26}\text{Al}/^{27}\text{Al}$ was homogeneous throughout the analyzed volume and that there was no loss of radiogenic ^{26}Mg .

3.1.3. Grain OR1d2m-19

Another grain with a SN signature in its N and O isotopic ratios (Table 1) is grain OR1d2m-19. The data points on the “isochron” plot for this grain also fall on a line, but here the line has a positive intercept with the y -axis (Figure 3(b)). According to the simulations in the Appendix (Figure 20) this would happen if the Al contamination increases while the Mg contamination decreases. In this grain the Al and ^{26}Mg signals are not constant but decrease with depth but by far

not as much as ^{24}Mg (and ^{25}Mg) (Figure 3(a)). As shown in Figure 3(c), the $\delta^{25}\text{Mg}/^{24}\text{Mg}$ values increase with the $^{27}\text{Al}/^{24}\text{Mg}$ ratio (and, because of the decreasing ^{24}Mg signal, with depth) but level off at $\sim 3200\%$ toward the end, a much higher value than the average value of 1247% (Table 1). If we assume that the average of the last four points represents the value of the intrinsic Mg, we can calculate the abundances of the intrinsic Mg and contaminating Mg throughout the profile. Interestingly, not only the Mg contamination but also the intrinsic Mg decreases with depth, the latter by a factor of 4.9, whereas ^{26}Mg decreases by a factor of 2.84 and ^{27}Al by a factor of 2.22. We also subtracted the contaminant and intrinsic ^{26}Mg from the total ^{26}Mg in order to obtain the radiogenic ^{26}Mg , for the intrinsic Mg assuming $\delta^{26}\text{Mg}/^{24}\text{Mg} = 3200\%$, the value for $\delta^{25}\text{Mg}/^{24}\text{Mg}$. However, the radiogenic ^{26}Mg is so dominant that this correction is negligible. The decrease of ^{27}Al being slower than that of ^{26}Mg explains the positive y-axis intercept, because if we assume that the intrinsic $^{27}\text{Al}/^{26}\text{Mg}$ ratio is that at the beginning of the profile, the relative increase in this ratio with depth can be interpreted as the addition of Al contamination. In this interpretation, the true (and constant) $^{26}\text{Al}/^{27}\text{Al}$ ratio of this grain would be 0.349, derived from the slope of the line connecting the first data point in Figure 3(b) to the origin. The addition of Al contamination with increasing depth results in a decrease of this ratio or in increasing shifts to the right of the data points in Figure 3(b), leading to a shallower slope (corresponding to $^{26}\text{Al}/^{27}\text{Al} = 0.273$) of the correlation line. The ratio derived from the total grain measurement of 0.308 (Table 1) lies between these two values. On the other hand, it could be that the $^{26}\text{Al}/^{27}\text{Al}$ ratio changes from 0.349 to 0.276 throughout the profile. This might be indicated by the fact that Al contamination is expected to be larger at the exterior of the grain and an increase with depth is difficult to understand. However, there is no way we can distinguish between these two possibilities. To turn this conclusion around, we cannot claim any heterogeneity of the $^{26}\text{Al}/^{27}\text{Al}$ ratio in this grain because its apparent variation can also be explained by Al contamination.

3.1.4. Grain OR1d3m-27

The Al–Mg data of this grain differ from the previously discussed grains in several respects. First, the radiogenic ^{26}Mg is not as dominating as in other grains (Figure 4(a)). This is expressed by the fact that the $^{26}\text{Al}/^{27}\text{Al}$ ratio inferred from the whole grain measurement is smaller than those of the other grains (Table 1). Second, the ^{26}Mg signal is not parallel to the ^{27}Al signal (Figure 4(a)), resulting in data points on the “isochron” plot that are shifted to the right and are not on a straight line (Figure 4(b)). Let us address the first point. The ^{24}Mg profile is not parallel to that of ^{25}Mg , making it clear that there is considerable contamination with isotopically normal Mg. If we assume that the $^{25}\text{Mg}/^{24}\text{Mg}$ ratio at the end of the profile (corresponding to the highest $\delta^{25}\text{Mg}/^{24}\text{Mg}$ values in Figure 4(c)) is that of the intrinsic Mg, we can calculate the proportions of intrinsic and contaminating Mg. The thus obtained profile of intrinsic ^{24}Mg is shown in Figure 4(a). The short-time variations in that profile are the result of fluctuations in the $^{25}\text{Mg}/^{24}\text{Mg}$ ratios (most likely statistical) that have an enhanced effect on the calculated intrinsic ^{24}Mg (e.g., clearly seen at 800 s). Furthermore, if we assume that the $\delta^{26}\text{Mg}/^{24}\text{Mg}$ value of the intrinsic Mg is the same as the $\delta^{25}\text{Mg}/^{24}\text{Mg}$ value, we can correct the measured ^{26}Mg for this contribution to obtain the radiogenic ^{26}Mg ($^{26}\text{Mg}^*$ in Figure 4(a)). As will be shown below (Figure 7), the assumption that the $\delta^{26}\text{Mg}/^{24}\text{Mg}$ value

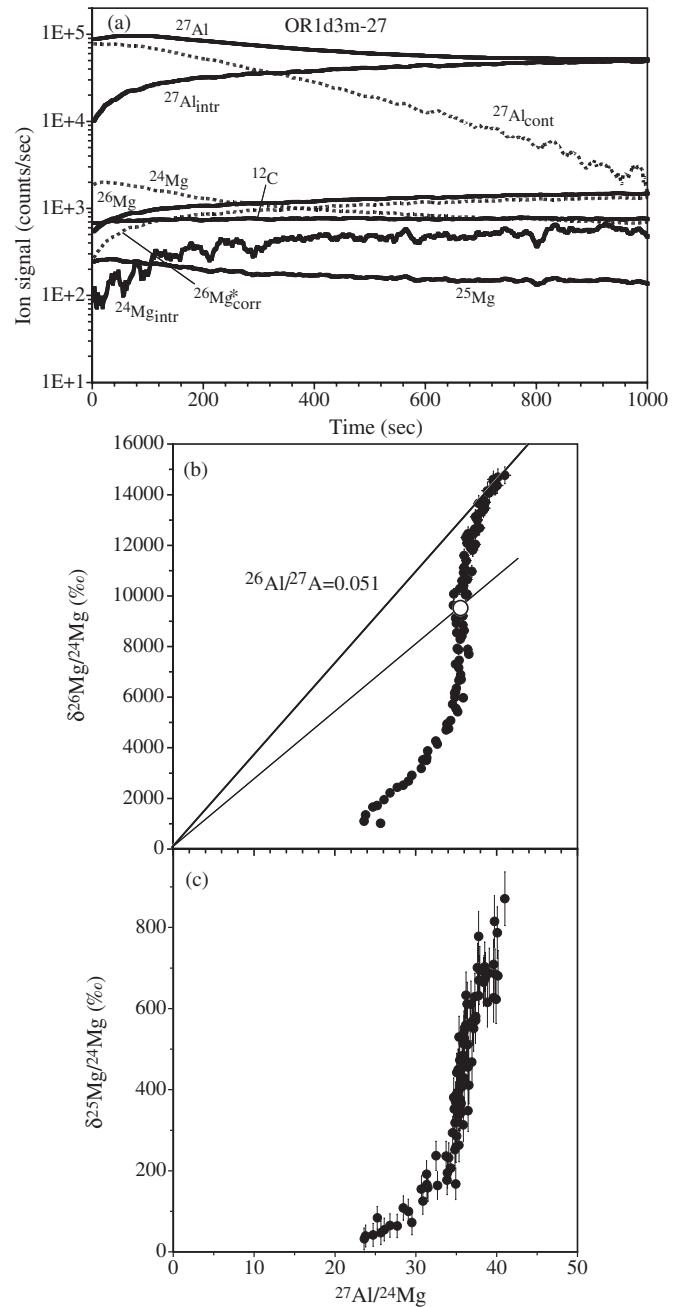


Figure 4. (a) Profiles of secondary ion signals for LD grain OR1d3m-27. The Al signal is decomposed into an intrinsic ($^{27}\text{Al}_{\text{intr}}$) and a contaminant ($^{27}\text{Al}_{\text{cont}}$) component. Also shown are profiles for the inferred intrinsic ^{24}Mg and radiogenic ^{26}Mg . See text for details. (b) Isochrone plot obtained from averages of five cycles. The large open circle represents the average ratios measured. The upper line represents the true intrinsic $^{26}\text{Al}/^{27}\text{Al}$ ratio if it is assumed that this ratio is constant throughout the profile and that the data points at the end of the profile are not affected by Al contamination any more. (c) Plot of $\delta^{25}\text{Mg}/^{24}\text{Mg}$ vs. $^{27}\text{Al}/^{24}\text{Mg}$.

of the intrinsic Mg is the same as the $\delta^{25}\text{Mg}/^{24}\text{Mg}$ value is highly uncertain. However, this uncertainty affects mostly the calculated $^{26}\text{Mg}^*$ at the beginning of the profile in Figure 4(a). It does not significantly affect the inferred intrinsic $^{26}\text{Al}/^{27}\text{Al}$ ratio, because $\delta^{26}\text{Mg}/^{24}\text{Mg}$ is much larger than $\delta^{25}\text{Mg}/^{24}\text{Mg}$ (Figures 4(b) and 4(c)) and the $^{26}\text{Al}/^{27}\text{Al}$ ratio is determined by the data points at the end of the profile.

The radiogenic ^{26}Mg to ^{27}Al ratios varies over a large range. If this were the result of $^{26}\text{Al}/^{27}\text{Al}$ heterogeneity, the ratio would

vary from 0.006 to 0.050. However, it is more likely that we are dealing with a large amount of Al contamination at the beginning of the profile (measurement). If we assume that the intrinsic $^{26}\text{Al}/^{27}\text{Al}$ ratio is 0.051 (corresponding to the slope of the upper line shown in Figure 4(b)), we can calculate the amounts of intrinsic ^{27}Al and contaminating ^{27}Al , as shown in Figure 4(a). As we can see, the ^{27}Al contamination falls off steeply, whereas the intrinsic ^{27}Al asymptotically approaches the total ^{27}Al . It is interesting that the ratio of the ^{27}Al contamination to the ^{24}Mg contamination is fairly constant at ~ 12 . Thus, it seems that the Al and Mg contaminations are related to one another, although we cannot think of a likely compound with this Al/Mg ratio. The grain appears to represent a combination of the two cases we consider in the Appendix. Neither the intrinsic Mg nor intrinsic Al are constant and the grain has contamination from both Al and Mg. The $^{26}\text{Al}/^{27}\text{Al}$ ratio might be somewhat higher than the value of 0.051 we assumed. As can be seen in Figure 4(b), the data points just turned to be aligned with a line through the origin but possibly could rise a little above this line. It is unfortunate that the measurement was terminated at 1000 s. If it were continued a little longer we would have been able to see whether we would indeed have reached a constant $^{26}\text{Mg}/^{27}\text{Al}$ ratio. Still, it seems that the ratio of 0.051 is not very far off the true intrinsic $^{26}\text{Al}/^{27}\text{Al}$ ratio. It is definitely higher than the ratio of 0.035, obtained from the whole grain measurement (Table 1) and corresponding to the slope of the line drawn from the origin to the average values in Figure 4(b). Likewise, the largest $\delta^{25}\text{Mg}/^{24}\text{Mg}$ value of $\sim 800\%$ is larger than the whole-grain average of 391‰ (Table 1).

3.1.5. Grain OR1d4m-16

This grain best represents the case shown in Figure 21: the ^{24}Mg and ^{25}Mg signals are fairly constant, whereas the ^{27}Al and ^{26}Mg signals strongly increase with depth (Figure 5(a)). However, the $^{26}\text{Mg}/^{27}\text{Al}$ ratio varies and becomes constant only in the final portion of the profile. This results in an “isochron” plot for which data points for most of the range of $^{27}\text{Al}/^{24}\text{Mg}$ ratios are shifted to the right of a straight line through the origin; only for high $^{27}\text{Al}/^{24}\text{Mg}$ ratios do the data points plot on such a line (Figure 5(b)). Again, this behavior is most likely not the result of (large) variations in the initial $^{26}\text{Al}/^{27}\text{Al}$ ratio but the result of Al contamination. As for the previous grain, we assume the last part of the profile to give the intrinsic $^{26}\text{Mg}/^{27}\text{Al}$ ratios. In this grain, the radiogenic ^{26}Mg is so dominant that a correction for the non-radiogenic ^{26}Mg is negligible. The initial $^{26}\text{Al}/^{27}\text{Al}$ ratio derived from this last part is 0.586. This corresponds to the upper line in Figure 5(b). The lower line through the average values gives a $^{26}\text{Al}/^{27}\text{Al}$ ratio of 0.482, the result of the whole-grain measurement (Table 1). The $^{25}\text{Mg}/^{24}\text{Mg}$ ratio of this grain is normal (Table 1 and Figure 5(c)), in contrast to the other grains discussed here, which show variable ^{25}Mg excesses, ranging up to 3200‰ in grain OR1d2m-19 (Figure 3(c)).

3.1.6. Grain OR1d4m-20

The reason we discuss this grain here is not that its profile represents a special case but that this grain has the highest $\delta^{26}\text{Mg}/^{24}\text{Mg}$ value and highest inferred $^{26}\text{Al}/^{27}\text{Al}$ ratio measured to date (Jadhav et al. 2013) in any presolar graphite grain (Hynes & Gyngard 2009). The $^{26}\text{Mg}/^{27}\text{Al}$ ratio in this grain is fairly constant (Figure 6(a)) and almost half of the data points in the “isochron” plot lie on a straight line whose slope corresponds

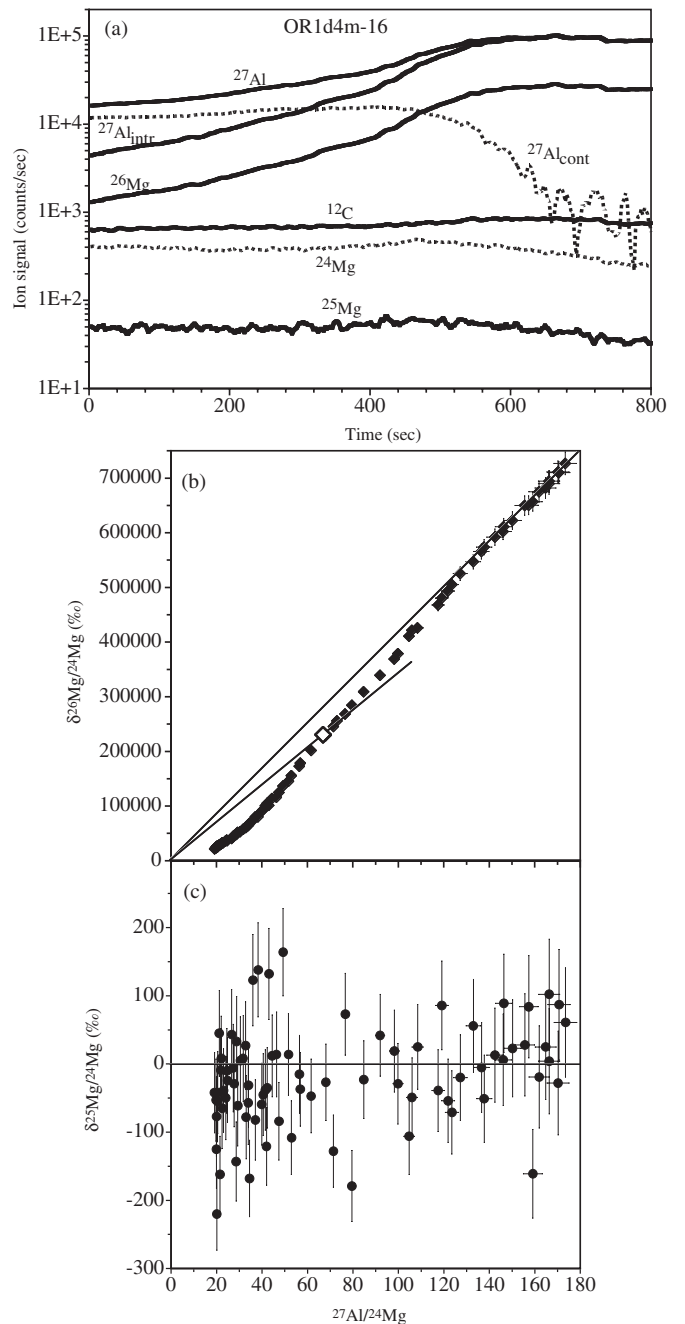


Figure 5. (a) Profiles of secondary ion signals for LD grain OR1d4m-16. As in Figure 4(a), the Al signal is decomposed into an intrinsic ($^{27}\text{Al}_{\text{intr}}$) and a contaminant ($^{27}\text{Al}_{\text{cont}}$) component. (b) Isochrone plot obtained from averages of five cycles. The large open diamond represents the average ratios measured. The upper line is a fit through the data points with the highest ratios and is believed to represent the true intrinsic $^{26}\text{Al}/^{27}\text{Al}$ ratio of the grain. (c) Plot of $\delta^{25}\text{Mg}/^{24}\text{Mg}$ vs. $^{27}\text{Al}/^{24}\text{Mg}$. In contrast to the previously shown grains, this grain does not have any ^{25}Mg excess.

to a $^{26}\text{Al}/^{27}\text{Al}$ ratio of 0.736 (Figure 6(b)). Deviation from this line can be explained by Al contamination. The average of the data points in Figure 6(b) give a $^{26}\text{Al}/^{27}\text{Al}$ ratio of 0.699, the value obtained by the whole-grain measurement (Table 1). The highest $\delta^{26}\text{Mg}/^{24}\text{Mg}$ value in the profile of 4.4×10^6 is higher than the average shown in the table; the same is true for the $\delta^{25}\text{Mg}/^{24}\text{Mg}$ value (Figure 6(c) and Table 1).

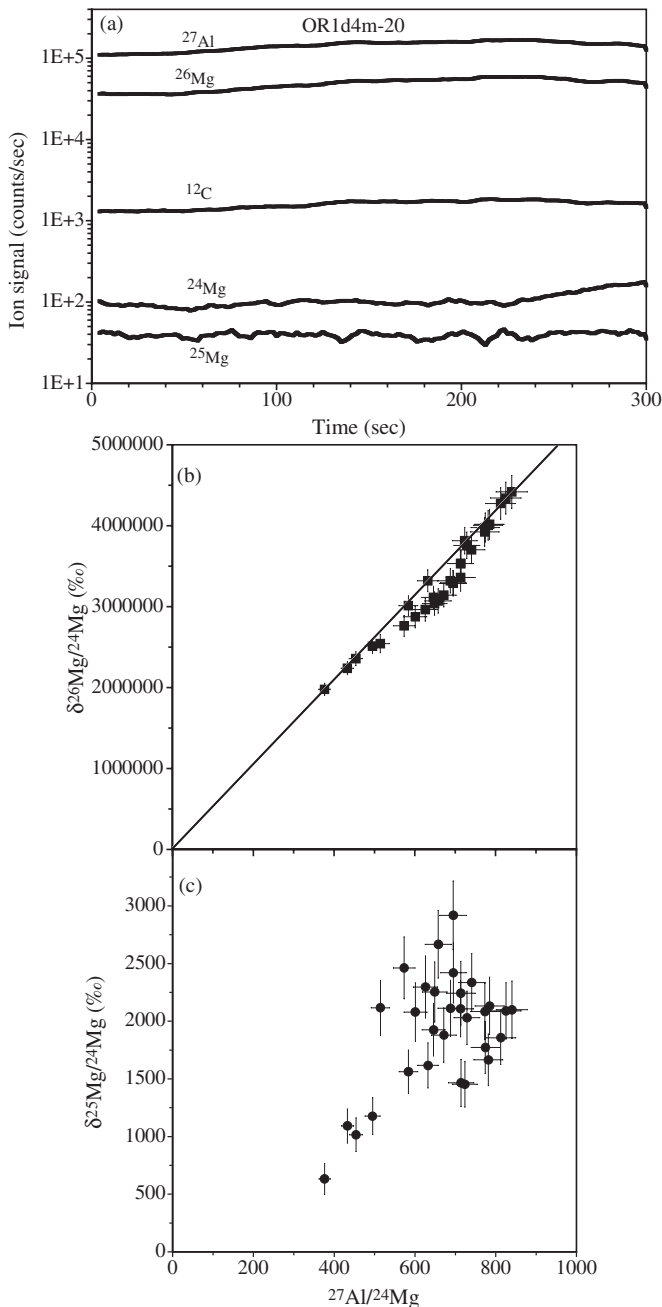


Figure 6. Profiles and isotope correlation plots for LD grain OR1d4m-20. This grain has an inferred $^{26}\text{Al}/^{27}\text{Al}$ ratio of 0.74, the largest ever measured in a presolar graphite grain.

3.1.7. Retention of Radiogenic ^{26}Mg

The essentially perfect correlation lines for grain OR1d2m-18 (Figure 2(b)) and OR1d2m-19 (Figure 3(b)) indicate that radiogenic ^{26}Mg is retained quantitatively and no loss or redistribution of radiogenic ^{26}Mg has taken place. Even in the grains without perfect correlation lines we argued that contamination with Al is responsible for deviations from straight correlation lines. In grains OR1d4m-16 (Figure 5(b)) and OR1d4m-20 (Figure 6(b)) the points with the highest $\delta^{26}\text{Mg}/^{24}\text{Mg}$ values and $^{27}\text{Al}/^{24}\text{Mg}$ ratios lie on straight lines through the origin. In addition, the corresponding $^{26}\text{Al}/^{27}\text{Al}$ ratios are among the highest seen in presolar grains, higher than any SN models predict. It is

clear that also in these two grains no substantial redistribution of radiogenic ^{26}Mg has taken place.

3.1.8. Supernova Models and Grains with High Inferred $^{26}\text{Al}/^{27}\text{Al}$ Ratios

Although the goal of this paper is not a detailed comparison of the grain data with SN models (see Jadhav et al. 2013 for a more detailed discussion), we want to make a short comment about graphite grains with extremely high $^{26}\text{Al}/^{27}\text{Al}$ ratios. The last two grains discussed here, OR1d4m-16 and OR1d4m-20, have inferred $^{26}\text{Al}/^{27}\text{Al}$ ratios of 0.586 and 0.736, respectively. Except for the Ni zone (see below), these ratios are higher than the highest theoretical ratios in any SN model. The highest ratios calculated in the models are achieved in the He/N zone, where proton capture on ^{25}Mg produces ^{26}Al . The maximum ratios in the Woosley & Weaver (1995), Rauscher et al. (2002), and Heger (<http://webusers.physics.umn.edu/~alex/sollo03/>) models are fairly similar, they range from 0.31 to 0.41 in models of $13 M_{\odot}$ to $25 M_{\odot}$. However, we note that these ratios are not constant throughout the He/N zone but usually decrease from the maximum to about half its value with decreasing internal mass in the zone. The maximum $^{26}\text{Al}/^{27}\text{Al}$ ratios calculated in the SN models by Limongi & Chieffi (2003, 2006) are even lower, ranging from 0.03 to 0.09. In the Rauscher et al. $15 M_{\odot}$ model, the $^{26}\text{Al}/^{27}\text{Al}$ ratio is 1.7 in the Ni zone. This is a consequence of the low ^{27}Al abundance in this zone. The ^{26}Al abundance in the Ni zone is only 40% of the highest ^{26}Al abundance in the He/N zone. Furthermore, the Ni zone is much narrower than the He/N zone so that the total mass of ^{26}Al is $7.1 \times 10^{-7} M_{\odot}$ in the Ni zone but $6.6 \times 10^{-6} M_{\odot}$ in the Ni zone. Furthermore, it is unclear how much of the innermost zone can be mixed into the outer He/C and He/N zones. For example, in order to explain the ^{28}Si excesses in SiC X grains and LD graphite grains, less than 0.1% of the Si/S zone needs to be admixed to the He/C and He/N zones. It is therefore extremely unlikely that the Ni zone contributes significantly to ^{26}Al in SN grains and the ^{26}Al in the grains must dominantly come from the He/N zone. However, not only do SN model predictions for the He/N fail to account for the highest $^{26}\text{Al}/^{27}\text{Al}$ ratios observed in presolar grains, but not all the material in the grains with high $^{26}\text{Al}/^{27}\text{Al}$ ratios can come from the He/N zone. In order to explain the C, N, and O isotopic ratios in these grains, material from the He/C zone (and possibly other zones) has to be mixed with material from the He/N zone, lowering the theoretical $^{26}\text{Al}/^{27}\text{Al}$ ratio even more, as has been discussed before for presolar SiC grains of type X (Lin et al. 2010).

Another observation about graphite grains with high $^{26}\text{Al}/^{27}\text{Al}$ ratios is that they have normal $^{25}\text{Mg}/^{24}\text{Mg}$ ratios or excesses in ^{25}Mg . In the He/N zone, ^{25}Mg is destroyed by proton capture during the production of ^{26}Al , and SN models predict a ^{25}Mg deficit in this zone (Figure 7). However, as can be seen in the figure, ^{25}Mg depletion also extends through almost the entire He/C zone. Only at the bottom of this zone and in the underlying O/C zone are ^{25}Mg excesses predicted. This means that mostly material from these layers has to be mixed with He/N material to achieve normal $^{25}\text{Mg}/^{24}\text{Mg}$ or ^{25}Mg excesses. This is additional evidence for the same conclusion reached previously on the basis of correlated hotspots (high concentrations) of ^{15}N and ^{18}O inside of LD graphite grains (Groopman et al. 2012). For the grains discussed here, we have made corrections for the intrinsic ^{26}Mg by assuming that the intrinsic $\delta^{26}\text{Mg}/^{24}\text{Mg}$ value is the same as the $\delta^{25}\text{Mg}/^{24}\text{Mg}$ value. As can be seen in Figure 7, there is considerable uncertainty in this assumption because these two

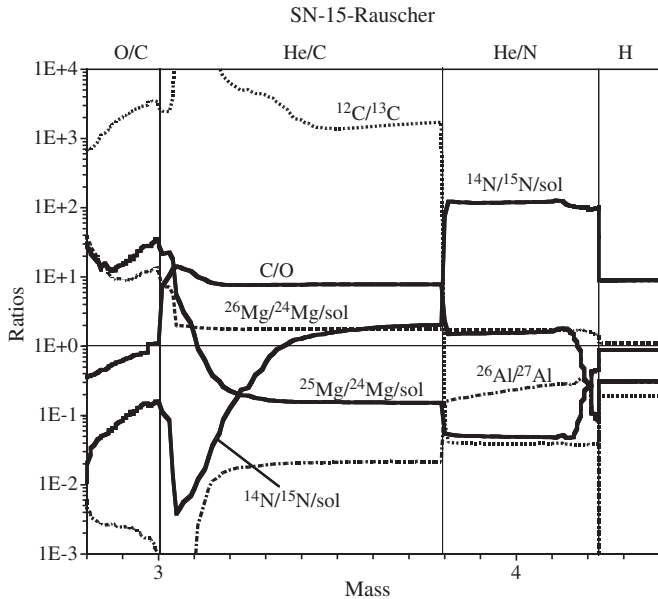


Figure 7. Isotopic and elemental ratios predicted for the interior zones in the $15 M_{\odot}$ SN model by Rauscher et al. (2002). The different zones of the SN are labeled according to Meyer et al. (1995) based on the most abundant elements present in each zone. All isotopic ratios except the $^{26}\text{Al}/^{27}\text{Al}$ ratio are normalized to the solar ratios. The $^{25}\text{Mg}/^{24}\text{Mg}$ ratio is lower than solar throughout the He/N zone and most of the He/C zone. These are the only SN zones with $\text{C} > \text{O}$.

values are the same in only a thin layer. In most grains discussed here, the radiogenic ^{26}Mg is so dominating that the correction for intrinsic ^{26}Mg is negligible. The exception is grain OR1d3m-27, where we obtained an inferred $^{26}\text{Al}/^{27}\text{Al}$ ratio of 0.051. If we assume that the $\delta^{26}\text{Mg}/^{24}\text{Mg}$ value of the intrinsic Mg is three times as high as the $\delta^{25}\text{Mg}/^{24}\text{Mg}$ value of 800‰ instead of the same, the inferred $^{26}\text{Al}/^{27}\text{Al}$ ratio is reduced to 0.046.

3.2. Ca–K System

3.2.1. Grain OR1f3m-9

Large excesses in ^{41}K in presolar graphite grains indicative of the initial presence of ^{41}Ca are not very common and are usually found in LD grains (Amari et al. 1996; Hynes & Gyngard 2009). Grain OR1f3m-9 is a HD graphite grain. Its N, O, Si, and Ca isotopic ratios do not provide a clear signature of a SN origin, but this grain has a large ^{41}K excess. This is shown in Figures 8(a) and (b). In Figure 8(a) we plotted also the calculated profile of ^{41}K if K had a normal $^{41}\text{K}/^{39}\text{K}$ ratio. As in most of the grains for which we discussed the Al–Mg system, the parent isotope ^{40}Ca is fairly constant and the spread in the $^{40}\text{Ca}/^{39}\text{K}$ ratio and $\delta^{41}\text{K}/^{39}\text{K}$ (Figure 8(b)) is generated by K contamination decreasing with depth. The correlation line in Figure 8(b) has a positive intercept with the x -axis, similar to the case shown in Figure 2(b). As discussed in the Appendix and as we argued in the case of grain OR1d2m-18 for the Al–Mg system, this shift of the correlation line indicates contamination with ^{40}Ca at the beginning of the profile (i.e., at low $^{40}\text{Ca}/^{39}\text{K}$ ratios). Because this contamination causes larger shifts to higher $^{40}\text{Ca}/^{39}\text{K}$ ratios at low ratios than at high ratios, the slope of the correlation line in Figure 8(b) is larger than the true slope. If we assume that the highest data points are not affected by Ca contamination, we can draw a line through the origin and the average of the highest six data points and obtain an inferred $^{41}\text{Ca}/^{40}\text{Ca}$ ratio

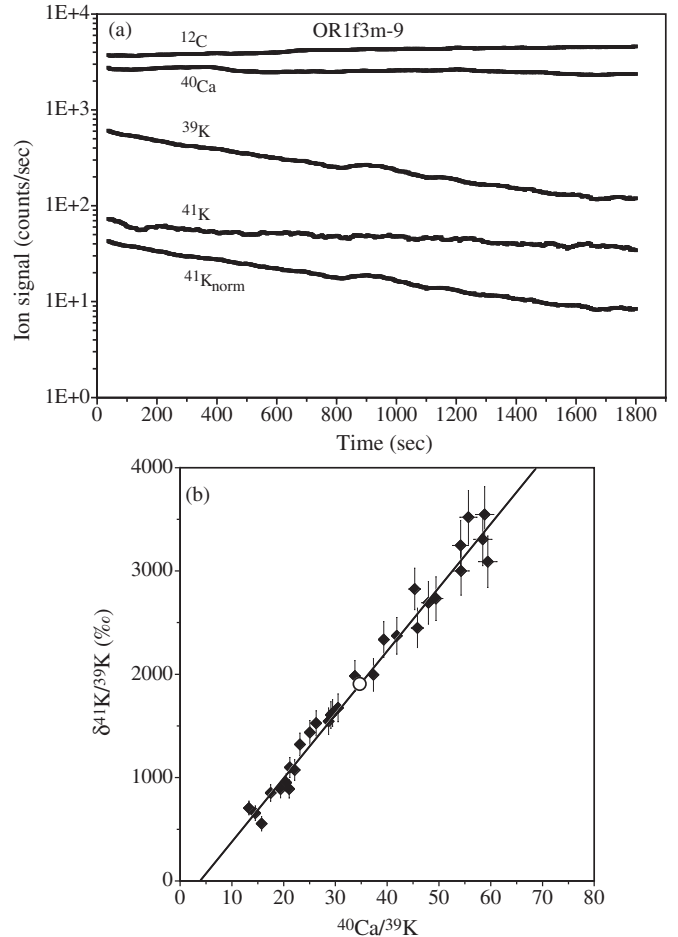


Figure 8. (a) Profiles of secondary ion signals for HD grain OR1f3m-9. Also shown is a profile for ^{41}K if the $^{41}\text{K}/^{39}\text{K}$ ratio were normal. (b) Isotope correlation plot of $\delta^{41}\text{K}/^{39}\text{K}$ vs. $^{40}\text{Ca}/^{39}\text{K}$ obtained from averages of ten cycles. The correlation line intercepts the x -axis. The large open circle represents the average ratios measured.

of 4.07×10^{-3} . This is only marginally higher than the ratio of 3.89×10^{-3} , obtained from the average $^{40}\text{Ca}/^{39}\text{K}$ ratio and $\delta^{41}\text{K}/^{39}\text{K}$ values (the large open circle in Figure 8(b)). Both values are much larger than what is expected from AGB models (Wasserburg et al. 1995; Nittler et al. 2008), but are within the range predicted for Type II SNe (Rauscher et al. 2002), indicating a SN origin for this grain. However, the almost normal N, O, Mg, and Si isotopic ratios in this grain remain puzzling.

3.2.2. Grain OR1f2m-o68

This grain is also a HD graphite grain. Its ^{15}N excess and large Ca and Ti isotopic anomalies (Table 1) indicate a SN origin. However, in contrast to many SN grain that have ^{28}Si excesses, this grain has large excesses in ^{29}Si and ^{30}Si . It thus resembles a very rare type of SiC grains, called C grains (Amari et al. 1999; Croat et al. 2010; Hoppe et al. 2010, 2012), which have large ^{29}Si and ^{30}Si excesses and SN signatures in other isotopic ratios. This grain has even larger $\delta^{41}\text{K}/^{39}\text{K}$ and inferred $^{41}\text{Ca}/^{40}\text{Ca}$ than grain OR1f3m-9 (Table 1). As in the previous grain, there is a large amount of K contamination decreasing with depth (Figure 9(a)) that is the cause of the large range in the data points of the “isochron” plot (Figure 9(b)). The correlation line misses the origin by only a small amount and there is a very small difference between the inferred $^{41}\text{Ca}/^{40}\text{Ca}$ ratio of

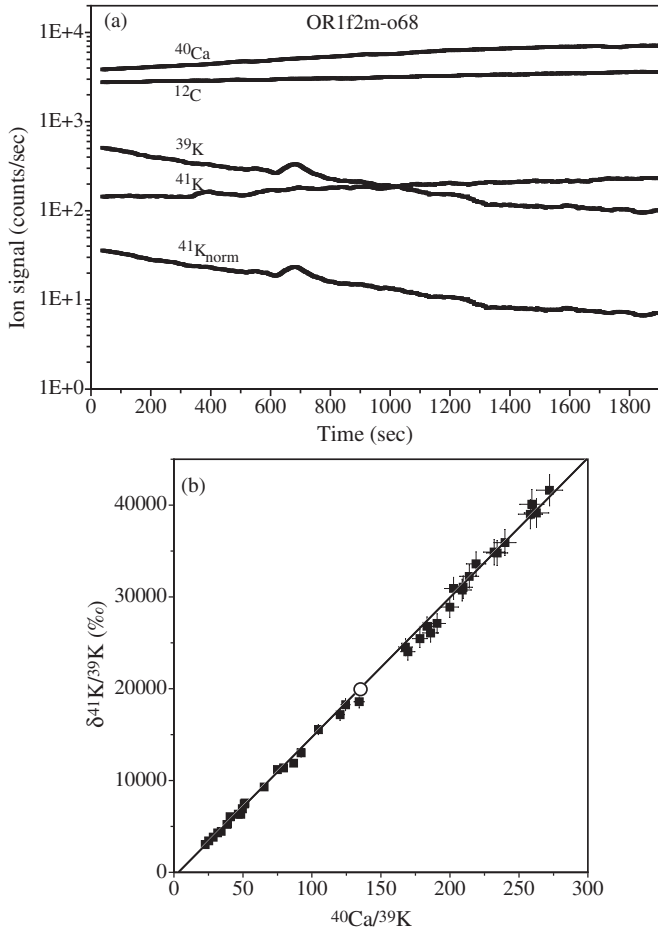


Figure 9. (a) Profiles of secondary ion signals for HD grain OR1f2m-068. Also shown is a profile for ^{41}K if the $^{41}\text{K}/^{39}\text{K}$ ratio were normal. (b) Isotope correlation plot obtained from averages of ten cycles. The correlation line goes almost through the origin. The large open circle represents the average ratios measured.

1.03×10^{-2} , obtained from the average values (open circle in Figure 9(b)) and the ratio of 1.06×10^{-2} , obtained from the highest four data points. From the profiles it is not clear whether the contamination has leveled off at the end of the profile. If not, the $^{40}\text{Ca}/^{39}\text{K}$ and $\delta^{41}\text{K}/^{39}\text{K}$ might even extend to higher values, but the inferred $^{41}\text{Ca}/^{40}\text{Ca}$ ratio is not likely to change much.

3.2.3. Retention of Radiogenic ^{41}K

In these two grains with evidence for ^{41}Ca the almost perfect correlation in the “isochron” plots indicates that the radiogenic ^{41}K is essentially retained quantitatively, similar to radiogenic ^{26}Mg in some of the grains discussed above. This observation opens the question where the contaminating K is located. Given the fact that radiogenic ^{41}K is retained in the graphite structure of the grain, we can safely exclude that the contaminating K invaded this structure. HD graphite grains are fairly compact, thus it is unlikely that K infiltrated pore spaces in the graphite. The contaminating K probably originally resided on the surface of the grains and was mixed into the surface layer of the grains through atomic collisions with the primary beam (“ion beam mixing”). It is also possible that K contamination had built up on the grain between Al–Mg and Ca–K analysis. Potassium is an ubiquitous contaminant. In addition, because the rastered primary beam covers the whole grain during analysis,

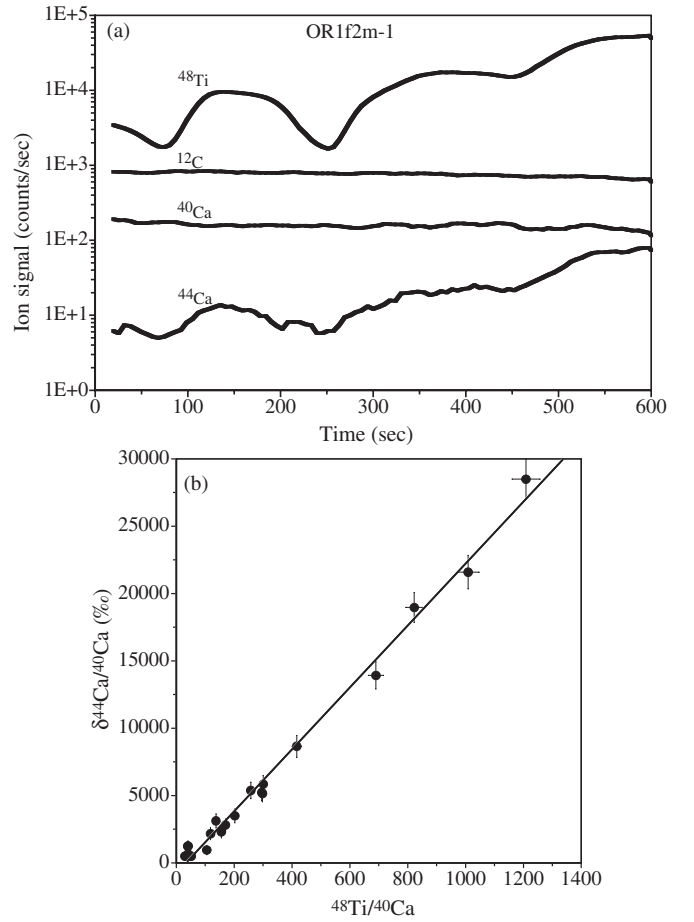


Figure 10. (a) Profiles of secondary ion signals for HD grain OR1f2m-1. The ^{48}Ti signal shows large variations, indicating the presence of TiC subgrains. These variations are accompanied by variations in ^{44}Ca from the decay of initial ^{44}Ti . (b) Isotope correlation plot of $\delta^{44}\text{Ca}/^{40}\text{Ca}$ vs. $^{48}\text{Ti}/^{40}\text{Ca}$ obtained from averages of five cycles. The data points lie close to a single line that goes almost through the origin.

contamination on the sides is still present while the beam sputters away contamination on the top surface.

3.3. Ti–Ca System

3.3.1. Grain OR1f2m-1

For the Al–Mg and Ca–K systems the parent element (Al and Ca) usually remains fairly constant throughout the profiles and the variation in the parent to daughter element ratio is caused by varying contamination with the daughter element (Mg and K). The situation is fundamentally different for the Ti–Ca system. Here, ^{40}Ca is constant, whereas ^{48}Ti varies wildly because of the presence of TiC subgrains. This is clearly seen in the profile of HD grain OR1f2m-1 (Figure 10(a)). During the analysis the primary beam sputtered through several subgrains, although we cannot tell how many because at a given time (depth) there could be several TiC grains on the exposed cross section of the grain. There is a good correlation between $\delta^{44}\text{Ca}/^{40}\text{Ca}$ and $^{48}\text{Ti}/^{40}\text{Ca}$ (Figure 10(b)). The correlation line has a small intercept with the x -axis. Because of the errors on the highest data points, within errors there is no difference in the $^{44}\text{Ti}/^{48}\text{Ti}$ ratio inferred from a line through the highest three points and the origin, and the value of 4.42×10^{-4} obtained from the average whole grain measurement (Table 1). However, the highest $\delta^{44}\text{Ca}/^{40}\text{Ca}$ value of almost 30,000‰ is much larger than the average. Evidence

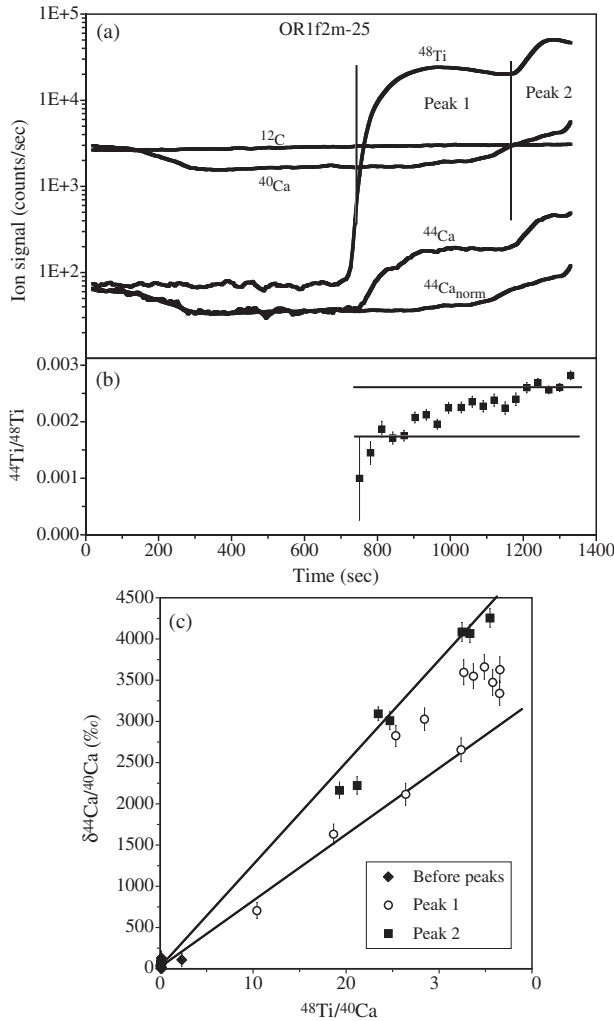


Figure 11. (a) Profiles of secondary ion signals for HD grain OR1f2m-25. Also shown is a profile for ^{44}Ca if the $^{44}\text{Ca}/^{40}\text{Ca}$ ratio were normal. The analyzed volume contains at least two TiC subgrains. (b) Inferred $^{44}\text{Ti}/^{48}\text{Ti}$ ratios obtained from averages of five cycles for the region with the internal TiC subgrains. The two horizontal lines correspond to the two lines in panel (c). (c) Isotope correlation plot of $\delta^{44}\text{Ca}/^{40}\text{Ca}$ vs. $^{48}\text{Ti}/^{40}\text{Ca}$ for different regions in the analyzed volume of the grain (panel a). The data points do not lie on a single line and differ for the two regions indicated in panel (a).

for the initial presence of ^{44}Ti is proof of a SN origin (Hoppe et al. 1996; Nittler et al. 1996; Timmes et al. 1996). As is the case with most HD graphite grains (Hoppe et al. 1995; Jadhav et al. 2013), the N, O, and Si isotopic ratios are normal, most likely the result of equilibration/contamination. The $^{12}\text{C}/^{13}\text{C}$ ratio is quite low (Table 1), indicating a substantial contribution from the He/N zone. The grain has a ^{49}Ti excess, typical of SN grains (Travaglio et al. 1999; Lin et al. 2002; Besmehn & Hoppe 2003; Jadhav et al. 2013).

3.3.2. Grain OR1f2m-25

This is another HD grain with no SN signatures in N and O. The larger ^{30}Si deficit and the high $^{12}\text{C}/^{13}\text{C}$ ratio are in agreement with expectations for a SN origin. Furthermore, this grain has a ^{41}K excess, indicating initial ^{41}Ca , and has a larger ^{49}Ti excess than the previous grain (Table 1). Also this grain shows the presence of internal TiC subgrains (Figure 11(a)). What is remarkable is the low Ti concentration in the portion of the graphite grain without TiC. The $^{48}\text{Ti}/^{40}\text{Ca}$ ratio there

is 0.07, corresponding to a Ti/Ca ratio of 0.092 if we assume normal isotopic ratios. The profile in Figure 11(a) shows a lower $^{48}\text{Ti}/^{40}\text{Ca}$ ratio because the ion signals are not corrected for differences in relative ion yields. A Ti/Ca ratio of 0.092 is still higher than the solar system ratio of 0.039 (Anders & Grevesse 1989; Lodders 2003). In SN models the Ti/Ca ratio is close to solar in the He/N and He/C zones. Thus, if the graphite mostly samples material from these zones, there appears to be a Ti/Ca fractionation by a factor of ~ 2.4 .

In contrast to the previous grain, the data points in the “isochron” plot do not lie on a straight line (Figure 11(c)). There is a difference between the points from the areas we label Peak 1 and Peak 2 in Figure 11(a). The line with the lower slope in Figure 11(c) corresponds to an inferred $^{44}\text{Ti}/^{48}\text{Ti}$ ratio of 1.78×10^{-3} and the upper line corresponds to a ratio of 2.69×10^{-3} . In Figure 11(b) we plot the inferred $^{44}\text{Ti}/^{48}\text{Ti}$ ratios for individual data points in the Peak 1 and Peak 2 regions. The two horizontal lines indicate the ratios obtained for the two lines in Figure 11(c). As can be seen in Figure 11(b), there is a steady increase of the data points as a function of time (depth in the sample). For grains containing initial ^{26}Al we explained deviation from a straight correlation line by invoking contamination with Al. This does not appear to be a likely explanation in the present case, because only contamination with Ti can shift the data points to the right in the “isochron” plot of Figure 11(c). The Ti abundance in the TiC-free area is very low. The amount of contaminating Ti in the region of Peak 1 would have to be at least 20% of the intrinsic Ti. This is a factor of 50 higher than the Ti in the TiC-free region. In addition, in other graphite grains without TiC subgrains and low uniform Ti contents, we do not see any evidence for Ti contamination of this magnitude. A possible explanation for the fact that data points do not plot on a line in Figure 11(c) is loss or redistribution of radiogenic ^{44}Ca . However, we think that this is also unlikely. We saw that radiogenic ^{26}Al and ^{41}K are retained in the graphite grains. It is difficult to see why radiogenic ^{44}Ca should not be retained in TiC subgrains. During the decay of ^{44}Ti into ^{44}Ca via ^{44}Sc , both by electron capture, the recoil energy of the ^{44}Ca nucleus is much too low for ^{44}Ca to be expelled from the TiC subgrain. The remaining possibility is that we are dealing with heterogeneity in the $^{44}\text{Ti}/^{48}\text{Ti}$ ratio among different TiC subgrains. We remind the reader that TiC subgrains formed independently before the formation of the graphite and were included into the growing host grain (Bernatowicz et al. 1991; Croat et al. 2003). It is quite possible that TiC subgrains formed in different environments and thus had different isotopic compositions. Titanium carbide subgrains have larger ^{18}O excesses than the host grain but also display a range of $^{18}\text{O}/^{16}\text{O}$ ratios (Stadermann et al. 2005). These variations in the $^{18}\text{O}/^{16}\text{O}$ ratios had been interpreted to be the result of different degrees of isotopic equilibration with a less anomalous environment. However, it is also possible that different TiC grains originally had different $^{18}\text{O}/^{16}\text{O}$ ratios. This makes it quite likely that TiC subgrains in a given host grain can have different initial $^{44}\text{Ti}/^{48}\text{Ti}$ ratios. We have to emphasize that at this time we cannot prove this fact unambiguously and cannot absolutely exclude the possibility of redistribution of radiogenic ^{44}Ca . To do this one would have to study the diffusive behavior of Ca in TiC. We plan to investigate whether there are variations in Ti isotopic ratios involving the stable Ti isotopes among TiC subgrains within a given graphite grain. In the study by Stadermann et al. (2005), three TiC subgrains showed identical Ti isotopic ratios, the same as the ratios obtained from the whole-grain measurement.

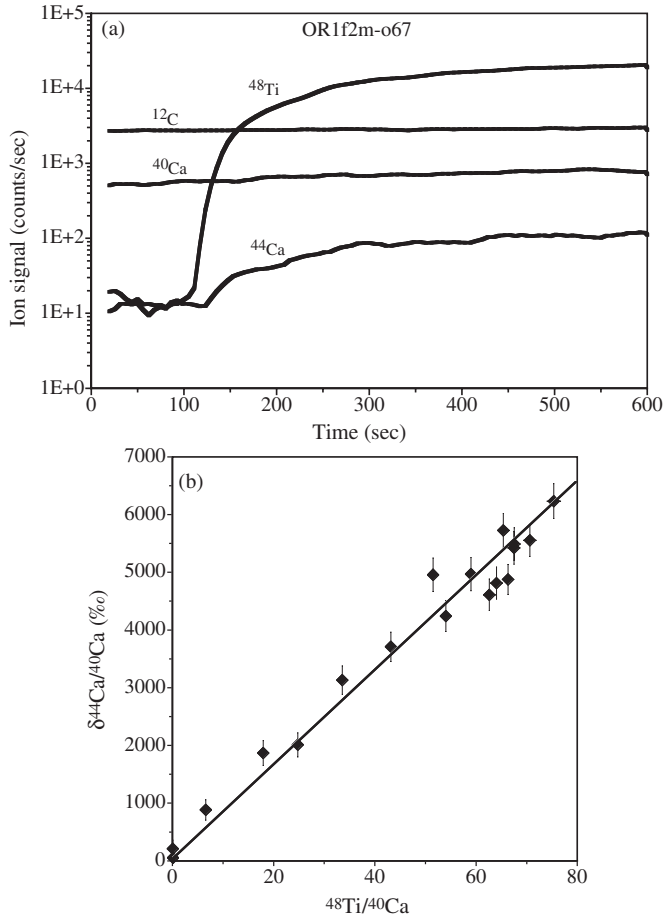


Figure 12. (a) Profiles of secondary ion signals for HD grain OR1f2m-o67. The large rise in the ^{48}Ti signal indicated the presence of one or several TiC subgrains. (b) Isotope correlation plot of $\delta^{44}\text{Ca}/^{40}\text{Ca}$ vs. $^{48}\text{Ti}/^{40}\text{Ca}$ obtained from averages of five cycles. Within errors, the data points lie close to a single line that goes through the origin.

3.3.3. Grain OR1f2m-o67

We include this grain because it has very peculiar isotopic compositions (Table 1). It has a very small $^{12}\text{C}/^{13}\text{C}$ ratio, a ^{15}N excess, a fairly high inferred $^{26}\text{Al}/^{27}\text{Al}$ ratio, a large ^{29}Si deficit but ^{30}Si excess. Titanium anomalies are not very large but the ^{50}Ti excess is larger than the ^{49}Ti excess. These are not unambiguous SN signatures, but there is clear evidence for the initial presence of ^{44}Ti and therefore the grain must have a SN origin. Figure 12(a) shows the Ca–Ti profiles for this grain. As in the previous grain, the Ti signal is quite low before sputtering by the primary beam exposed TiC subgrains. There is no sign of individual subgrains but it is doubtful that the long duration of the ^{48}Ti signal indicates the presence of a single huge TiC subgrain. From the ratio of the $^{48}\text{Ti}^+$ signal to the $^{12}\text{C}^+$ signal we can estimate what fraction of the graphite cross section is taken up by TiC. The positive ion yield of Ti is roughly a thousand times higher than that of C. The $^{48}\text{Ti}^+/^{12}\text{C}^+$ ratio at the end of the profile is 6.5, which means that approximately 1% of the surface area is covered by TiC. If the surface has the diameter of the graphite grain (12 μm), then the diameter of a single TiC grain would have to be 1.2 μm . Such a large TiC grain has never been observed. It is more likely that the high ^{48}Ti signal is produced by many subgrains exposed on the surface.

The data points in Figure 12(b) scatter somewhat around the correlation line but the deviations are marginal. We used only

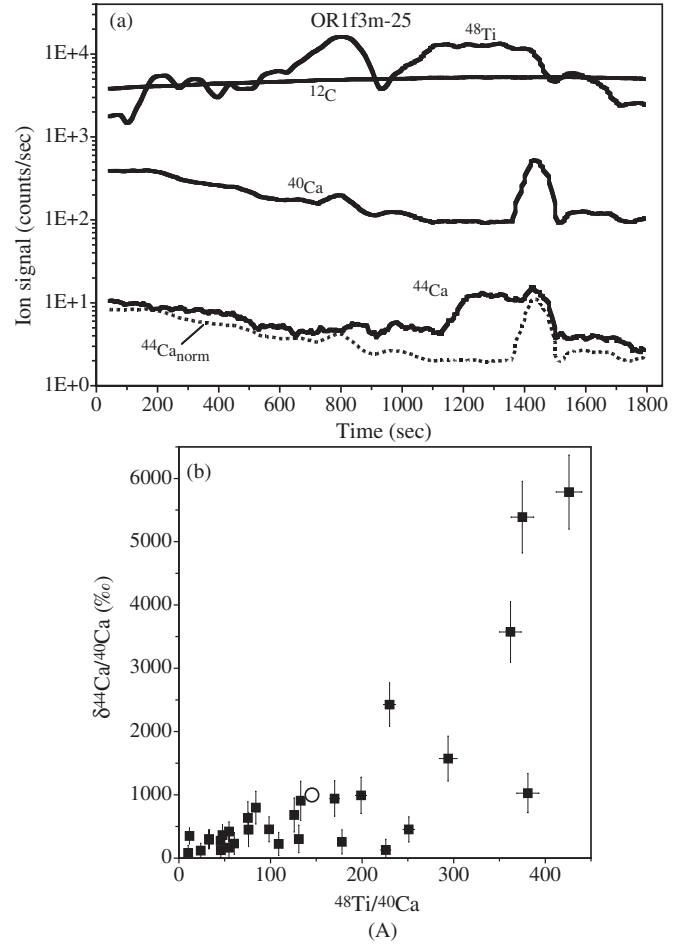


Figure 13. (A-a) Profiles of secondary ion signals for HD grain OR1f3m-25. Also shown is a profile for ^{44}Ca if the $^{44}\text{Ca}/^{40}\text{Ca}$ ratio were normal. The difference between $^{44}\text{Ca}_{\text{norm}}$ and the measured ^{44}Ca signal indicates large ^{44}Ca excesses. (A-b) Isotope correlation plot of $\delta^{44}\text{Ca}/^{40}\text{Ca}$ vs. $^{48}\text{Ti}/^{40}\text{Ca}$ obtained from averages of ten cycles. There exists a large scatter of the data points. The circle depicts the averages of the ratios. (B-a) Profiles of secondary ion signals for HD grain OR1f3m-25 as in (A-a). The vertical lines indicate regions with TiC subgrains. (B-b) $\delta^{44}\text{Ca}/^{40}\text{Ca}$ values obtained from averages of ten cycles along the measurement profile. (B-c) $^{48}\text{Ti}/^{40}\text{Ca}$ ratios along the measurement profile indicating the presence of TiC subgrains. (B-d) Inferred $^{44}\text{Ti}/^{48}\text{Ti}$ ratios along the measurement profile. There are large variations, expressing the lack of correlation between the $\delta^{44}\text{Ca}/^{40}\text{Ca}$ values and $^{48}\text{Ti}/^{40}\text{Ca}$ ratios plotted in panels (B-b) and (B-c). For example, the first ^{48}Ti peak has almost no ^{44}Ca excess, and consequently the inferred $^{44}\text{Ti}/^{48}\text{Ti}$ ratio is not very different from zero.

counting statistics to determine the errors for $\delta^{44}\text{Ca}/^{40}\text{Ca}$ and $^{48}\text{Ti}/^{40}\text{Ca}$ but because of changes of these values during the measurement the actual errors could be larger. In any case, the deviations are not large enough that we want to pursue this issue. From the correlation line we obtain an inferred $^{44}\text{Ti}/^{48}\text{Ti}$ ratio of 1.77×10^{-3} , the same value as obtained from the whole-grain measurement (Table 1).

3.3.4. Grain OR1f3m-25

While in this grain $\delta^{44}\text{Ca}/^{40}\text{Ca}$ values reach almost 6000‰ (Figure 13(A-b)), the scatter of the data points is much larger than in grain OR1f2m-25 (Figure 11(c)). Some regions with high $^{48}\text{Ti}/^{40}\text{Ca}$ ratios have no ^{44}Ca excess within errors. This grain has a ^{43}Ca excess (Table 1) and we have to ask how much of ^{44}Ca excesses could be intrinsic (non-radiogenic). Since some $\delta^{44}\text{Ca}/^{40}\text{Ca}$ values shown in Figure 13(A-b) are close to zero, the intrinsic ^{44}Ca excesses cannot be very high.

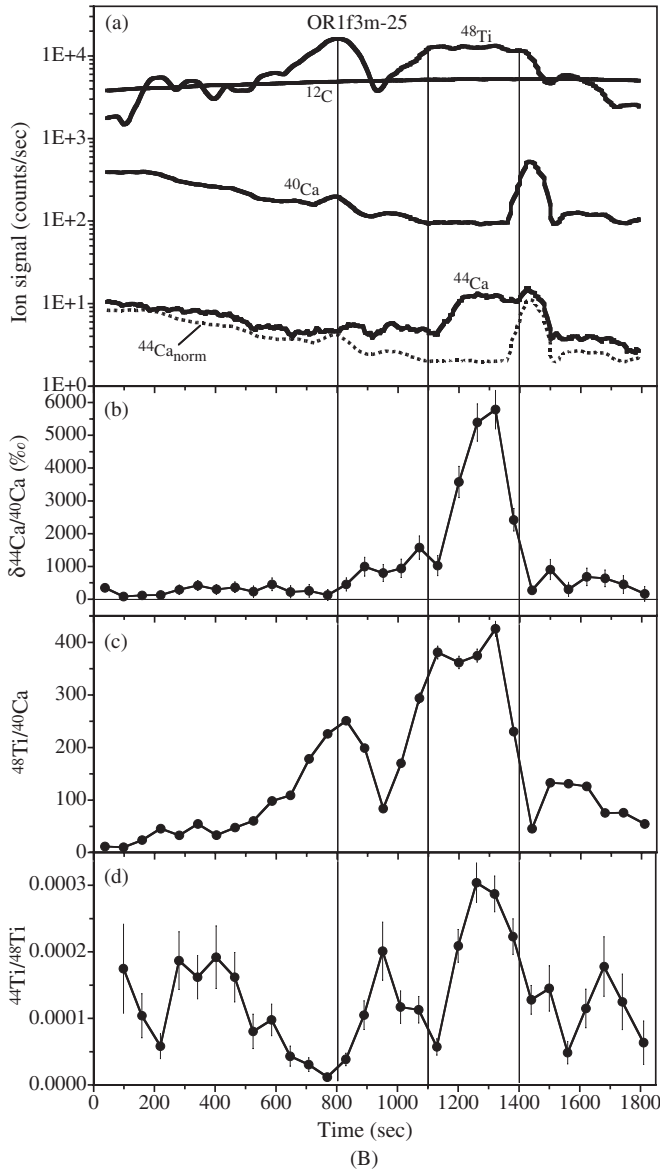


Figure 13. (Continued)

The condition $\delta^{44}\text{Ca}/^{40}\text{Ca} > \delta^{43}\text{Ca}/^{40}\text{Ca}$ has been taken as a sign that ^{44}Ca excesses originate from ^{44}Ti decay. In the He/C zone and interior zones of a type II SN, $^{42,43,44}\text{Ca}$ are produced by neutron capture. However, from the He/C zone through to the O/Si zones $\delta^{43}\text{Ca}/^{40}\text{Ca}$ values are at least a factor of five larger than $\delta^{44}\text{Ca}/^{40}\text{Ca}$ values; in the He/C and the outer layers of the O/C zone this factor is at least 10 (Rauscher et al. 2002). Thus, we estimate that the intrinsic $\delta^{44}\text{Ca}/^{40}\text{Ca}$ value is at most on the order of 50‰. Furthermore, the $\delta^{42}\text{Ca}/^{40}\text{Ca}$ (also $\delta^{43}\text{Ca}/^{40}\text{Ca}$) and some $\delta^{44}\text{Ca}/^{40}\text{Ca}$ values for $^{48}\text{Ti}/^{40}\text{Ca}$ ratios between 100 and 250 s agree with zero within 2σ errors. We will ignore possible intrinsic ^{44}Ca excesses; for our analysis it will not make any difference. As can be seen from the profile, TiC subgrains are encountered throughout most of the scan (Figure 13(A-a)). There are two regions with high ^{48}Ti signals, one around 800 s and the other extending from 1100 to 1400 s. These regions are indicated by the vertical lines in Figure 13(B). The second region is probably comprised of several subgrains, although the presence of several subgrains in the first region cannot be

excluded. There exists a large ^{44}Ca excess in the second region as demonstrated by the ^{44}Ca profile that exceeds the profile calculated under the assumption of a normal $^{44}\text{Ca}/^{40}\text{Ca}$ ratio. On a linear scale this is shown in Figure 13(B-b). However, what is puzzling is that this excess is large only in the later (inner) part of this region: while the $^{48}\text{Ti}/^{40}\text{Ca}$ ratio is high in most of the region (it becomes lower toward 1400 s because of the presence of a Ca-rich subgrain, Figure 13(B-c)), the $\delta^{44}\text{Ca}/^{40}\text{Ca}$ values are high only in the inner part. Furthermore, there is hardly any ^{44}Ca excess in the first region around 800 s (Figure 13(B-b)), where the $^{48}\text{Ti}/^{40}\text{Ca}$ ratio is high (Figure 13(B-c)). This lack of detailed correlations is reflected in Figure 13(B-d) where, as for grain OR1f2m-25 (Figure 11(b)), we plot the $^{44}\text{Ti}/^{48}\text{Ti}$ ratio inferred from the individual data point for $\delta^{44}\text{Ca}/^{40}\text{Ca}$ and $^{48}\text{Ti}/^{40}\text{Ca}$ (Figures 13(B-b) and (B-c)). We note that these data points are obtained from the sums over 10 cycles, whereas the profiles are obtained from running averages over 10 cycles. This is the reason that the profile in Figures 13(B-b)–(B-d) consists of fewer discrete points. There are large variations in the inferred $^{44}\text{Ti}/^{48}\text{Ti}$ ratio across the whole range of the profile. The maximum ratio is $(3.04 \pm 0.29) \times 10^{-4}$, whereas the average ratio obtained from the average $\delta^{44}\text{Ca}/^{40}\text{Ca}$ and $^{48}\text{Ti}/^{40}\text{Ca}$ values (open circle in Figure 13(A-b)) is 1.45×10^{-4} .

Again, we are faced with two choices: either radiogenic ^{44}Ca was redistributed from the TiC subgrains after ^{44}Ti decay, or we observe a range of different $^{44}\text{Ti}/^{48}\text{Ti}$ ratios in different TiC subgrains. While we cannot exclude the first possibility with certainty, it is most likely not the only explanation. Some grain(s) in the inner part of region two apparently retained the radiogenic ^{44}Ca , which results in a high $\delta^{44}\text{Ca}/^{40}\text{Ca}$ value and high inferred $^{44}\text{Ti}/^{48}\text{Ti}$ ratio. On the other hand, the grain(s) in region one must have lost essentially all radiogenic ^{44}Ca if the $^{44}\text{Ti}/^{48}\text{Ti}$ ratio was originally the same. It is difficult to understand how the radiogenic ^{44}Ca could have behaved so differently in different TiC subgrains enclosed in the same graphite host grain. The best way to investigate possible heterogeneity in different subgrains would be by isotopic imaging of the grain's cross section, which would allow one to distinguish between individual TiC subgrains. This has not been done so far. One reason is that graphite grains with large ^{44}Ca excesses from ^{44}Ti decay are quite rare (Hynes & Gyngard 2009). Furthermore, isotopic imaging is time consuming. Thus, one would like to establish that a grain has a ^{44}Ca excess before attempting isotopic imaging on that grain. Ideally, to reduce morphology effects, isotopic imaging should be done on microtome slices deposited on a flat substrate such as a Si wafer (Groopman et al. 2012) rather than on the whole grain. Again, preparation of such slices is a time consuming process. We hope that we will be able to undertake such a study in the future. At this time we tentatively conclude that different TiC subgrains can have different initial $^{44}\text{Ti}/^{48}\text{Ti}$ ratios.

3.3.5. Grain OR1d4m-9

While in this grain the N and O isotopic ratios have only marginal SN signatures, the grain has a fairly high inferred $^{26}\text{Al}/^{27}\text{Al}$ ratio and a clear ^{28}Si excess (Table 1). Even more pronounced than in the previous grain, the profiles show a ^{48}Ti peak at the beginning and three distinct peaks in the interior (Figure 14(A-a)). However, the data points also scatter in the $\delta^{44}\text{Ca}/^{40}\text{Ca}$ versus $^{48}\text{Ti}/^{40}\text{Ca}$ plot (Figure 14(A-b)). The ^{44}Ca excesses track the $^{48}\text{Ti}/^{40}\text{Ca}$ ratios (Figures 14(B-a)–(B-c)), however $\delta^{44}\text{Ca}/^{40}\text{Ca}$ values are higher in between and outside of the ^{48}Ti peak regions than would be expected from

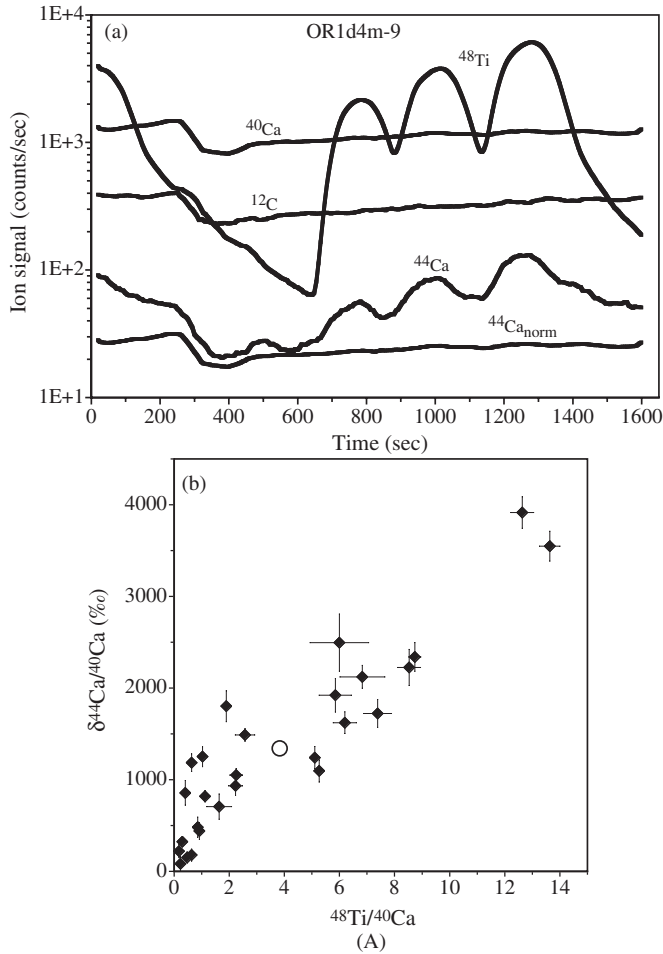


Figure 14. (A-a) Profiles of secondary ion signals for LD grain OR1d4m-9. Also shown is a profile for ^{44}Ca if the $^{44}\text{Ca}/^{40}\text{Ca}$ ratio were normal. There are several TiC subgrains present in the analyzed volume. (A-b) Isotope correlation plot of $\delta^{44}\text{Ca}/^{40}\text{Ca}$ vs. $^{48}\text{Ti}/^{40}\text{Ca}$ obtained from averages of ten cycles. There exists a large scatter of the data points. The circle depicts the averages of the ratios. (B-a) Profiles of secondary ion signals for HD grain OR1d4m-9 as in (A-a). The vertical lines indicate regions with TiC subgrains. (B-b) $\delta^{44}\text{Ca}/^{40}\text{Ca}$ values obtained from averages of ten cycles along the measurement profile. (B-c) $^{48}\text{Ti}/^{40}\text{Ca}$ ratios along the measurement profile indicating the presence of TiC subgrains. (B-d) Inferred $^{44}\text{Ti}/^{48}\text{Ti}$ ratios along the measurement profile. There are large variations. Although maxima in $\delta^{44}\text{Ca}/^{40}\text{Ca}$ values coincide with TiC subgrains, the highest inferred $^{44}\text{Ti}/^{48}\text{Ti}$ ratios are not in these regions.

the corresponding $^{48}\text{Ti}/^{40}\text{Ca}$ ratios. As a result, the inferred $^{44}\text{Ti}/^{48}\text{Ti}$ ratios are not highest in the regions of the ^{48}Ti peaks but are higher between the peaks (at 900 and 1130 s) and especially much higher at the end of the profile where $^{48}\text{Ti}/^{40}\text{Ca}$ ratios are very low but where $\delta^{44}\text{Ca}/^{40}\text{Ca}$ values are still substantial (Figures 14(B-b)–(B-d)). The $^{44}\text{Ti}/^{48}\text{Ti}$ ratios inferred in this way vary from 4.4×10^{-3} to 4.5×10^{-2} . The average obtained from the average $\delta^{44}\text{Ca}/^{40}\text{Ca}$ and $^{48}\text{Ti}/^{40}\text{Ca}$ values (Figure 14(A-b)) is 7.5×10^{-3} . This grain differs from grain OR1f3m-25, where the highest inferred $^{44}\text{Ti}/^{48}\text{Ti}$ ratio occurs in a region with TiC subgrains (although only in one of them). Again, the variations in the $^{44}\text{Ti}/^{48}\text{Ti}$ ratios could reflect variations in the ratio in different TiC subgrains or be the result of redistribution of radiogenic ^{44}Ca . In this grain there is some evidence in support of the latter possibility. In the right flanks of the ^{48}Ti peak at the beginning of the profile and the third of the peaks in the interior, the $\delta^{44}\text{Ca}/^{40}\text{Ca}$ values fall off less steeply than the $^{48}\text{Ti}/^{40}\text{Ca}$ (cf. Figures 14(B-b) and (B-c)). This could be the result of diffusion of the radiogenic ^{44}Ca from TiC

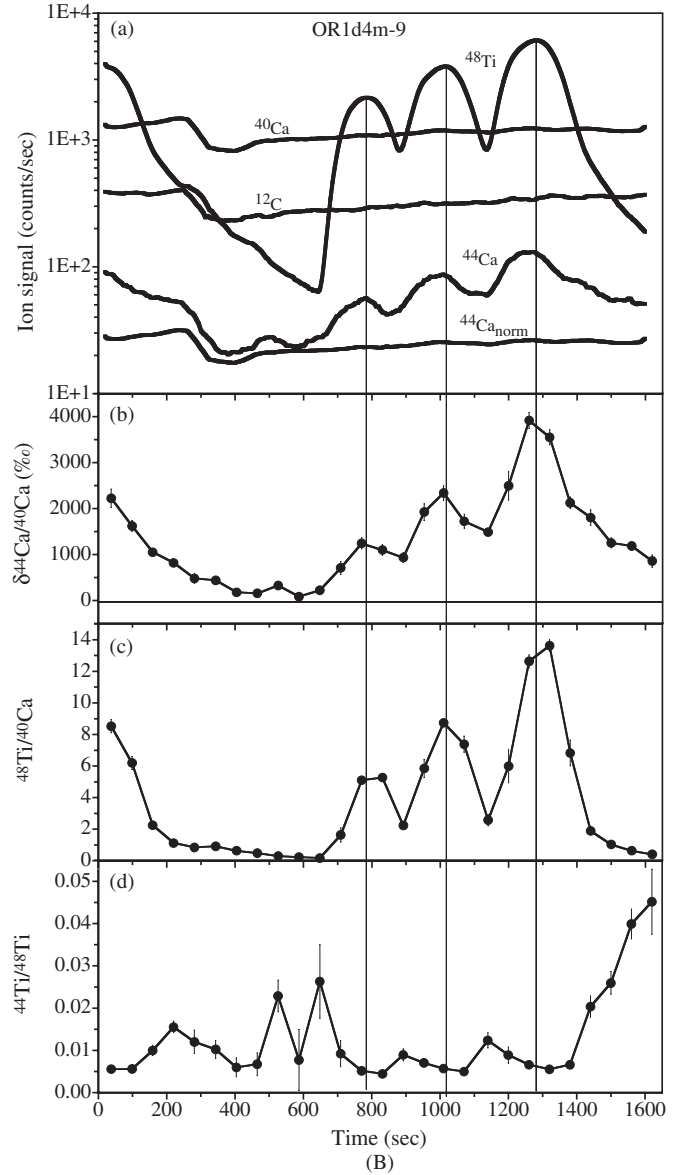


Figure 14. (Continued)

subgrains into the surrounding graphite. We hope that future imaging studies will be able to resolve this issue.

3.3.6. Grain OR1f3m-12

This grain has no SN signature in its N, O, Mg, and Si isotopic ratios (Table 1). However, it has $\delta^{44}\text{Ca}/^{40}\text{Ca} > \delta^{43}\text{Ca}/^{40}\text{Ca}$ and, according to our discussion of grain OR1f3m-25, some of the ^{44}Ca excess should be from ^{44}Ti decay. What is peculiar about this grain is that it does not have any internal TiC grains within the analyzed volume and the Ti content is low (Figure 15(a)). Also during the subsequent analysis of Ti isotopes no TiC subgrains were encountered. Figure 15(b) shows the $\delta^{44}\text{Ca}/^{40}\text{Ca}$ versus $^{48}\text{Ti}/^{40}\text{Ca}$ plot. Essentially all the scatter is consistent with the individual errors. A least squares fit forced to go through the origin gives the line shown in the plot and a chi square value of 1.3. As we mentioned earlier, the real errors could be somewhat larger than the errors based on counting statistics. The fit yields an inferred $^{44}\text{Ti}/^{48}\text{Ti}$ ratio of 2.3×10^{-2} . If there is an intrinsic ^{44}Ca excess, it would lower this ratio. If we assume that the intrinsic $\delta^{44}\text{Ca}/^{40}\text{Ca}$ value is 30%,

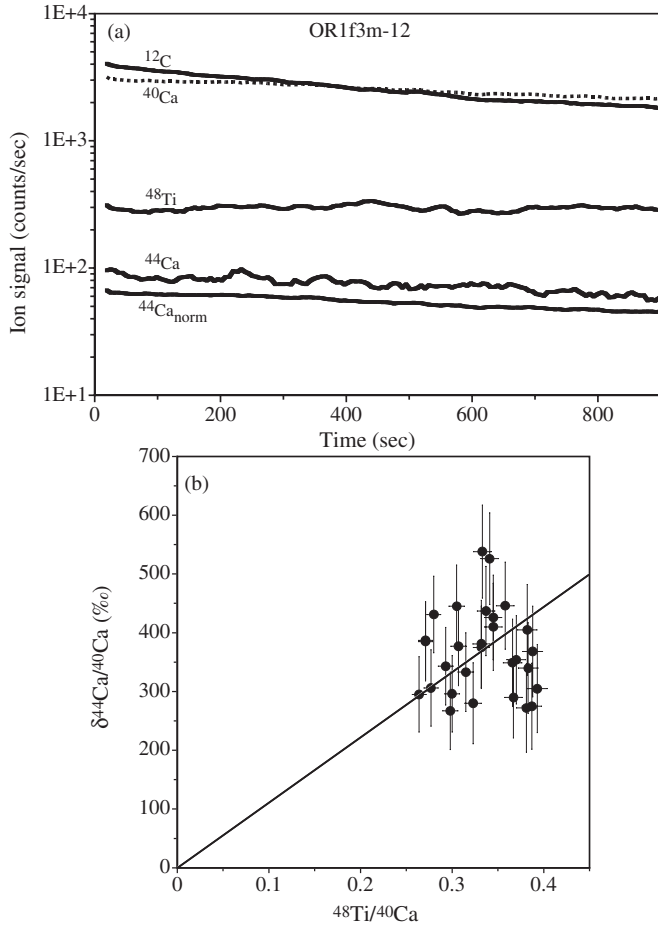


Figure 15. (a) Profiles of secondary ion signals for HD grain OR1f3m-12. Also shown is a profile for ^{44}Ca if the $^{44}\text{Ca}/^{40}\text{Ca}$ ratio were normal. There are no Ti-rich subgrains and the ^{48}Ti signal is very low. (b) Isotope correlation plot of $\delta^{44}\text{Ca}/^{40}\text{Ca}$ vs. $^{48}\text{Ti}/^{40}\text{Ca}$ obtained from averages of five cycles. In spite of the low $^{48}\text{Ti}/^{40}\text{Ca}$, this grain shows a ^{44}Ca excess.

20% of the $\delta^{43}\text{Ca}/^{40}\text{Ca}$ value (probably an upper value), then the $^{44}\text{Ti}/^{48}\text{Ti}$ ratio would be lowered to 2.1×10^{-2} . This value is still much higher than the ratio for any of the grains we previously discussed (Table 1). On the other hand, in the portion of grain OR1f2m-25 before the encounter with TiC subgrains, there is no apparent ^{44}Ca excess (Figure 11(a)). The $\delta^{44}\text{Ca}/^{40}\text{Ca}$ value for this region is $13 \pm 11\%$, essentially consistent with zero. The average $^{48}\text{Ti}/^{40}\text{Ca}$ ratio is 0.11, resulting in an upper limit of 5×10^{-3} for the $^{44}\text{Ti}/^{48}\text{Ti}$ ratio. It is ironic that this limit is higher than the ratios obtained in the regions of the subgrains, which show a clear ^{44}Ca excess (Figure 11(b)). It is peculiar that grain OR1f3m-12, the grain without any TiC subgrains has the highest inferred $^{44}\text{Ti}/^{48}\text{Ti}$ ratio, but we do not know exactly in which SN regions TiC subgrains and graphite grains formed. In SiC X grains, inferred $^{44}\text{Ti}/^{48}\text{Ti}$ ratios are roughly correlated with ^{28}Si excesses (Lin et al. 2010). Of the grains of this study, only OR1d4m-9 has a clear ^{28}Si excess, while some others are marginal (Table 1). Grain OR1f3m-12 has a modest ^{29}Si deficit, but no ^{30}Si deficit. If the grain obtained its ^{44}Ti from the Si/S region, it is expected to show a larger ^{28}Si excess (Lin et al. 2010). Thus, either Si was fractionated from Ti or the ^{44}Ti originated from the Ni core, which does not have any Si.

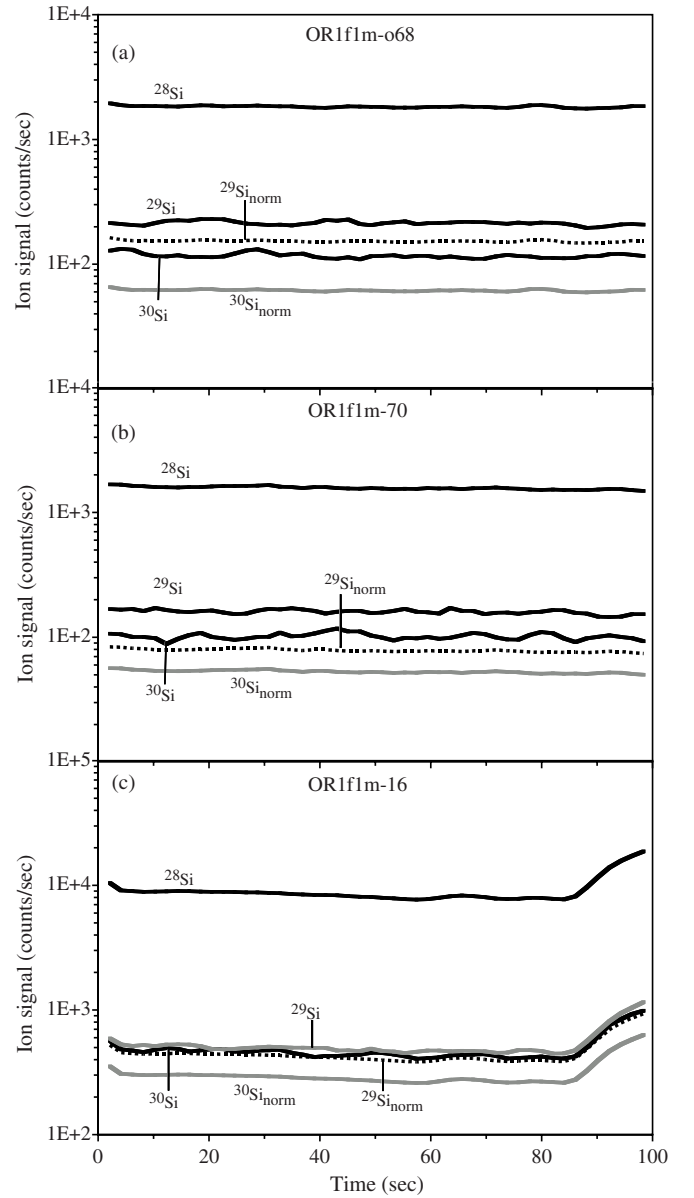


Figure 16. Profiles of Si secondary ion signals in three different HD graphite grains. Also shown are profiles for ^{29}Si and ^{30}Si if the $^{29}\text{Si}/^{28}\text{Si}$ and $^{30}\text{Si}/^{28}\text{Si}$ ratios were normal. There is no evidence for Si-rich subgrains in the first two graphite grains; the increase of the Si signal in the third grain, OR1f3m-16, indicates the presence of a subgrain.

3.4. Si Isotopes

This last section does not discuss the distribution of radiogenic daughters of short-lived isotopes but presents Si depth profiles of three unusual grains. These grains have large excesses in ^{29}Si and ^{30}Si . Recently, a new type of presolar SiC grains has been identified: C grains (Croat et al. 2010; Gyngard et al. 2010; Hoppe et al. 2010, 2012; Zinner et al. 2010a). They are believed to have a SN origin as evidenced by several other isotopic signatures, including the initial presence of ^{44}Ti . Some C grains have large ^{32}S excesses (Gyngard et al. 2010; Hoppe et al. 2010, 2012; Xu et al. 2012). The three graphite grains discussed here resemble C grains in their Si isotopic ratios (Table 1). Croat et al. (2010) identified SiC C grains as subgrains within a graphite grain from the Murchison HD fraction KFC1. In Figure 16, we show Si isotope depth profiles

of the three Orgueil graphite grains OR1f2m-o68, OR1f1m-70, and OR1f1m-16. We discussed grain OR1f2m-o68 in connection with its large ^{41}K excess implying the presence of initial ^{41}Ca . As can be seen in Figures 16(a) and (b), two grains do not have any subgrains. The excesses in ^{29}Si and ^{30}Si are uniformly distributed throughout the analyzed volume. The measurement of grain OR1f1m-16 appears to encounter a subgrain at the end of the profile, however, the rest of the profile shows the same ^{30}Si excess as the subgrain (Figure 16(c)). Grain OR1f2m-o68 has a ^{15}N excess, a high inferred $^{41}\text{Ca}/^{40}\text{Ca}$ ratio and large Ca and Ti anomalies, indicating a SN origin. Grain OR1f1m-70 also has a ^{15}N excess, however, the third grain does not have any SN signature in its N and O isotopic ratios. With the exception of one $3\ \mu\text{m}$ large grain (Amari et al. 1999), all SiC C grains identified so far are submicrometer in size. Furthermore, C grains are rare; their abundance is $\sim 1\%$ of all SiC grains (Gyngard et al. 2010; Hoppe et al. 2010, 2012; Xu et al. 2012). If more large graphite grains with C-grain Si isotopic signatures (OR1f2m-o68 was $15\ \mu\text{m}$ in diameter) are found, they might allow detailed isotopic studies of many elements and elucidate in more detail the origin of these grains.

4. CONCLUSIONS

The study of depth profiles into presolar graphite grains during isotopic analysis with the NanoSIMS allowed us to obtain isochron-like correlation plots for the Al–Mg, Ca–K, and Ti–Ca systems. Some grains show perfect correlation between $\delta^{26}\text{Mg}/^{24}\text{Mg}$ and $^{27}\text{Al}/^{24}\text{Mg}$, $\delta^{41}\text{K}/^{39}\text{K}$ and $^{40}\text{Ca}/^{39}\text{K}$, $\delta^{44}\text{Ca}/^{40}\text{Ca}$ and $^{48}\text{Ti}/^{40}\text{Ca}$, indicating homogeneous initial $^{26}\text{Al}/^{27}\text{Al}$, $^{41}\text{Ca}/^{40}\text{Ca}$, and $^{44}\text{Ti}/^{48}\text{Ti}$ ratios and quantitative retention of radiogenic ^{26}Mg , ^{41}K , and ^{44}Ca . Computer simulations showed that deviations from perfect correlation lines for the Al–Mg and Ca–K system can be explained by contamination with Al or isotopically normal Ca, respectively. However, in a couple of grains, the deviations in the depth profiles of the Ti–Ca system indicate either diffusive redistribution of radiogenic ^{44}Ca or heterogeneity in the initial $^{44}\text{Ti}/^{48}\text{Ti}$ ratios within the grains.

Silicon isotope depth profiles in three grains with large ^{29}Si and ^{30}Si excesses show no Si-rich subgrains and uniform Si isotopic ratios in two of the graphite grains. The third grain contained an apparent Si-rich subgrain, but the anomalous Si isotopic ratios in the subgrain are the same as in the rest of the graphite host.

Thus, in the absence of isotopic imaging studies of grains to ascertain their internal distribution of isotopic and elemental compositions, isotopic depth profiles and isochron-type plots give a first-order insight into internal heterogeneities. Depth profiles can indicate possible diffusion of radiogenic isotopes from subgrains into the host grain that has not been observed before. They are also useful in determining contamination levels in the grains and obtaining improved values for isotopic anomalies and inferred ratios of short-lived to stable nuclides.

We thank Peter Hoppe for a careful review of the manuscript. We also thank Tim Smolar for his assistance with the NanoSIMS. This work was supported by NASA grant NNX11AH14G to E.Z.

APPENDIX

We performed a series of simulations in order to explore the effects of contamination with the parent and daughter elements on the “isochron” plots. For demonstration we use the Al/Mg

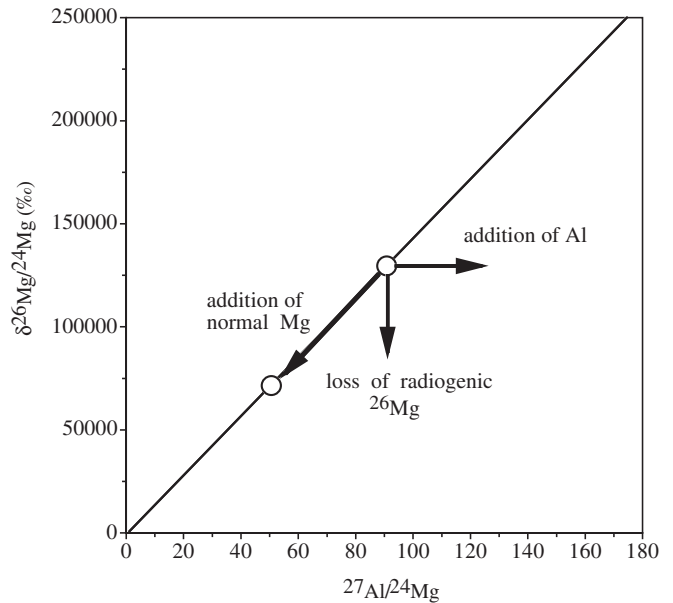


Figure 17. Schematic isotope correlation plot of $\delta^{26}\text{Mg}/^{24}\text{Mg}$ vs. $^{27}\text{Al}/^{24}\text{Mg}$ demonstrating the effect of addition of Mg and Al, and the loss of radiogenic ^{26}Mg .

system but the following investigation holds for any other system with a short-lived radioisotope. Figure 17 shows the $\delta^{26}\text{Mg}/^{24}\text{Mg}$ versus $^{27}\text{Al}/^{24}\text{Mg}$ plot for a sample with a large constant initial $^{26}\text{Al}/^{27}\text{Al}$ ratio. If the Al and Mg concentrations in the sample are uniform, the system is characterized by a single point. If isotopically normal Mg is added, the point is shifted toward the origin. On the other hand, if Al is added, the point is shifted to the right. Loss of radiogenic ^{26}Mg shifts the point down. If in different regions of the sample different amounts of normal Mg are added, we will obtain a series of points that all lie on a straight line through the origin and the original data point.

We show this in the first simulation where we assumed constant Al with an initial $^{26}\text{Al}/^{27}\text{Al}$ (now $^{26}\text{Mg}^*/^{27}\text{Al}$) ratio of 0.2 ($^{26}\text{Mg}^*$ denotes radiogenic ^{26}Mg) and an initial and constant intrinsic isotopically normal Mg with $^{24}\text{Mg}/^{27}\text{Al} = 0.04$. To this we added varying amounts of isotopically normal Mg, simulating the variation we see in profiles such as that for grain OR1d2m-18 in Figure 2. Figure 18(a) shows the profiles of ^{27}Al , intrinsic ^{24}Mg , $^{26}\text{Mg}^*$ and the added isotopically normal ^{24}Mg (we call it henceforth Mg contamination) whose amount decreases linearly with cycle number. This contamination results in a wide range of $\delta^{26}\text{Mg}/^{24}\text{Mg}$ values and $^{27}\text{Al}/^{24}\text{Mg}$ ratios and a perfect correlation of the data points. We note that this does not have anything to do with the assumed linear dependence on the cycle number. In fact, any random distribution of contaminating Mg will result in a linear array. Uniform addition of normal Mg shifts the data points along the correlation line toward the origin (Figure 18(c)). On the other hand, uniform addition of Al results in a correlation with a smaller slope (Figure 18(c)).

Addition of Al in an amount that is proportional to the (varying) Mg contamination (Figure 19(a), case a) results in an “isochron” plot where the points are still perfectly correlated but where the correlation line intercepts the x-axis at a positive value (Figure 19(b), case a). This can be easily understood by the fact that the Al contamination is large, resulting in large horizontal shifts of the original data points, in a region where the Mg contamination is also large, corresponding to small

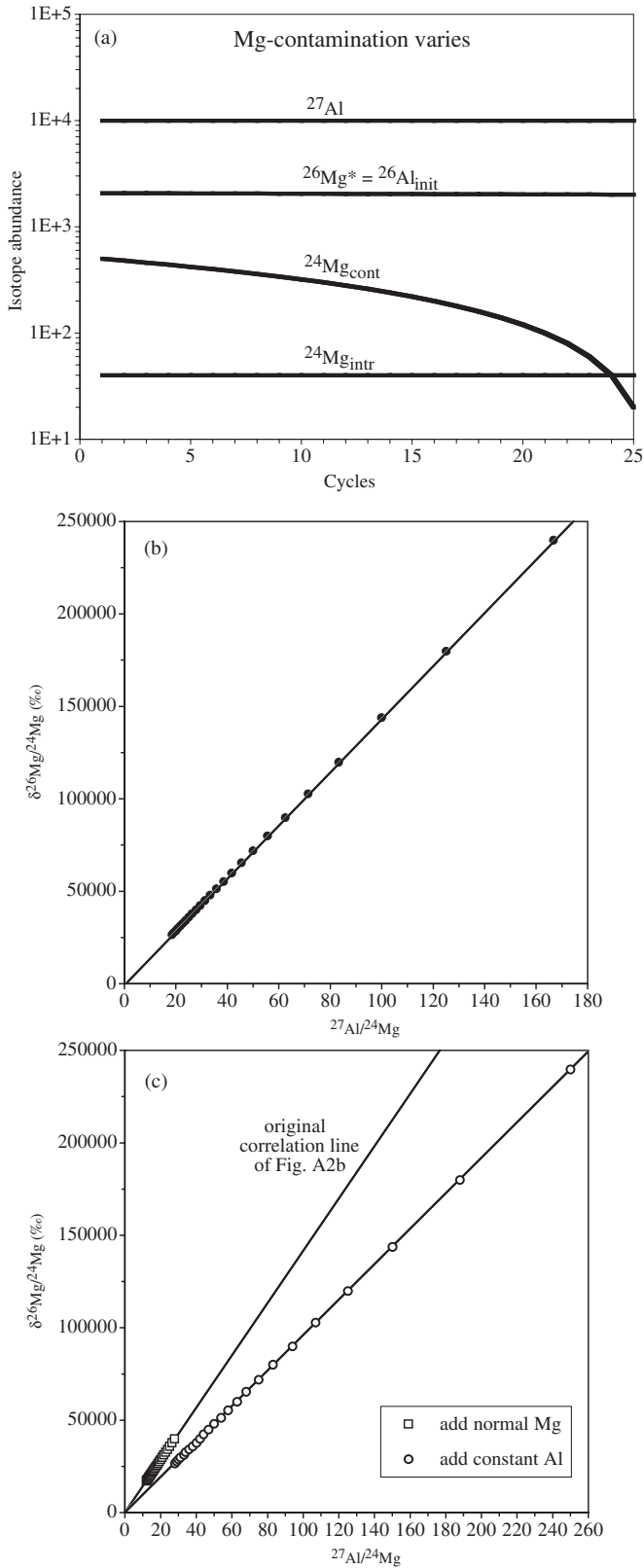


Figure 18. Results of a simulation of ^{26}Al decay and the effect of contamination with isotopically normal Mg and Al. See the text for details. (a) Profiles of isotopic concentrations with assumed constant $^{26}\text{Al}/^{27}\text{Al}$ ratio, constant intrinsic Al and Mg, and varying Mg contamination. (b) Isotope correlation plot of $\delta^{26}\text{Mg}/^{24}\text{Mg}$ vs. $^{27}\text{Al}/^{24}\text{Mg}$ obtained from the assumed profiles shown in panel (a). (c) Isotope correlation plots of the data points shown in panel (b) if constant isotopically normal Mg or constant Al is added.

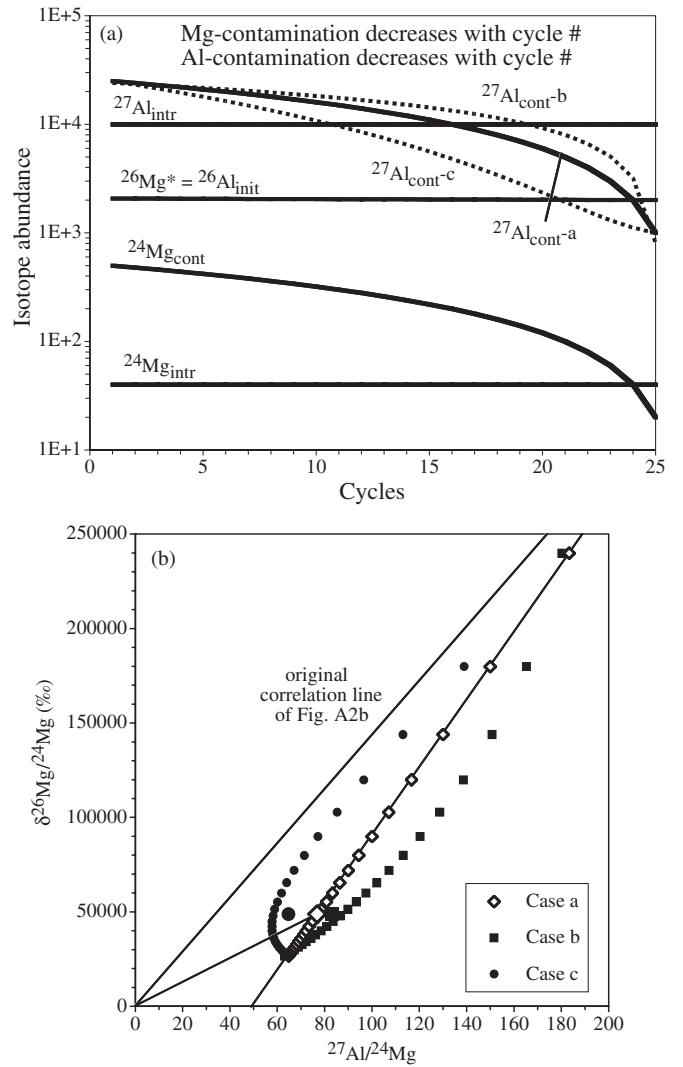


Figure 19. (a) Profiles of Al and Mg isotopes as in Figure 18(a). Also shown are three different assumed profiles of Al contamination that decrease with cycle number. See the text for details. (b) Isotope correlation plot of $\delta^{26}\text{Mg}/^{24}\text{Mg}$ vs. $^{27}\text{Al}/^{24}\text{Mg}$ showing the effects of the three assumed forms of Al contamination. Only the first Al contamination profile, which is a multiple of the Mg contamination profile, results in a straight correlation line that has a larger slope than the original and intercepts the x-axis.

$\delta^{26}\text{Mg}/^{24}\text{Mg}$ and $^{27}\text{Al}/^{24}\text{Mg}$ values. On the other hand, in a region with low Mg and Al contamination, corresponding to large $\delta^{26}\text{Mg}/^{24}\text{Mg}$ and $^{27}\text{Al}/^{24}\text{Mg}$ values, the horizontal shifts are small. We note that the slope of this line is larger than the original slope (Figure 18(b)) and is thus larger than the initial $^{26}\text{Mg}^*/^{27}\text{Al}$ ($^{26}\text{Al}/^{27}\text{Al}$) ratio. In order to be able to plot the Mg and Al contamination on a log scale, we assumed finite values for the smallest contamination contributions. If we would have assumed zero, the highest point in Figure 19(b) would be the same as that in Figure 18(b) and connecting this point with the origin would give us the original slope (and thus the initial $^{26}\text{Al}/^{27}\text{Al}$ ratio). With finite values for the minimum contamination, the point is shifted to the right as a comparison with the original correlation line shows. Thus, if the Al contamination is not zero anywhere in the sample, strictly speaking we cannot determine the original $^{26}\text{Al}/^{27}\text{Al}$ ratio. The ratio obtained from the whole grain measurement, i.e. from the total $\delta^{26}\text{Mg}/^{24}\text{Mg}$ and $^{27}\text{Al}/^{24}\text{Mg}$ values, is even

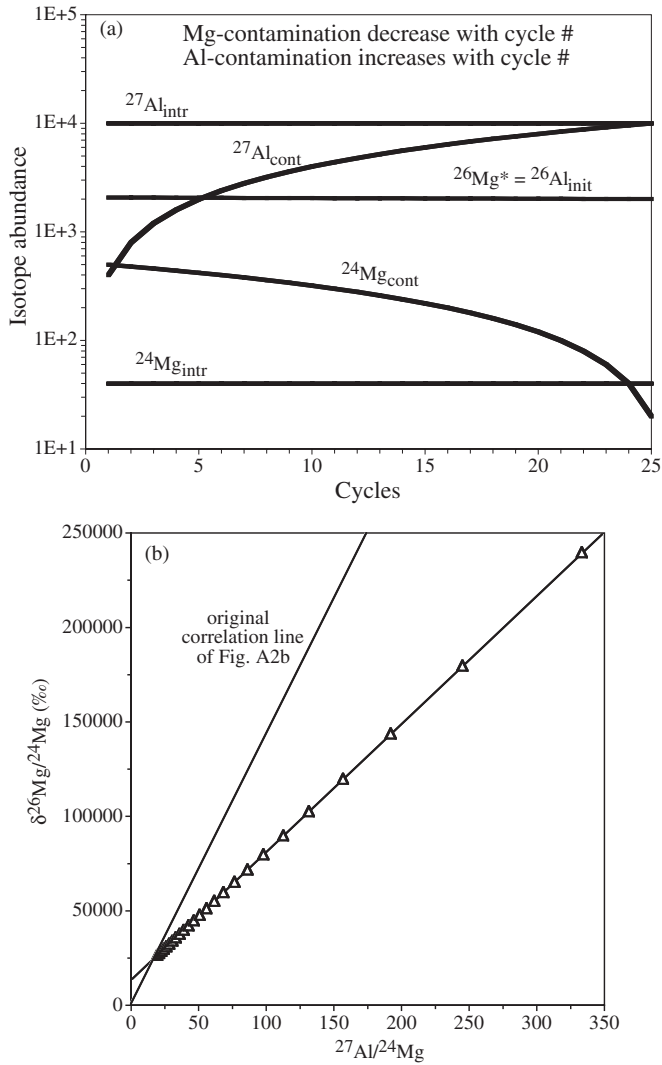


Figure 20. (a) Profiles of Al and Mg isotopes as in Figure 18(a). Also shown is an assumed profile of Al contamination that increases with cycle number. (b) Isotope correlation plot of $\delta^{26}\text{Mg}/^{24}\text{Mg}$ vs. $^{27}\text{Al}/^{24}\text{Mg}$ showing that the assumed Al contamination profile results in a straight correlation line that has a smaller slope than the original and intercepts the y-axis.

farther off. As can be seen in Figure 19(b), the slope of the line connecting the average of case a (the large open diamond) with the origin is much smaller than that of the original correlation line (without Al contamination) corresponding to the original intrinsic $^{26}\text{Al}/^{27}\text{Al}$ ratio. We explored two more cases where the Al contamination is not proportional to the Mg contamination. In case b the Al contamination is larger for increasing cycle numbers than in case a, in case c it is smaller (Figure 19(a)). These assumptions result in curved lines with different signs of curvature in the “isochron” plot (Figure 19(b)).

If, on the other hand, we add Al that uniformly increases with cycle number (Figure 20(a)), in other words, if we add the most Al where the Mg contamination is lowest and thus the original $^{27}\text{Al}/^{24}\text{Mg}$ ratio largest, the correlation line on the “isochron” plot intercepts the y-axis at a positive value and the slope is much smaller than the original slope (Figure 20(b)). Again, by assuming other shapes of the Al contamination, we can generate curved lines.

So far we assumed a uniform distribution of the original (intrinsic) ^{27}Al and of radiogenic ^{26}Mg . An alternative is to

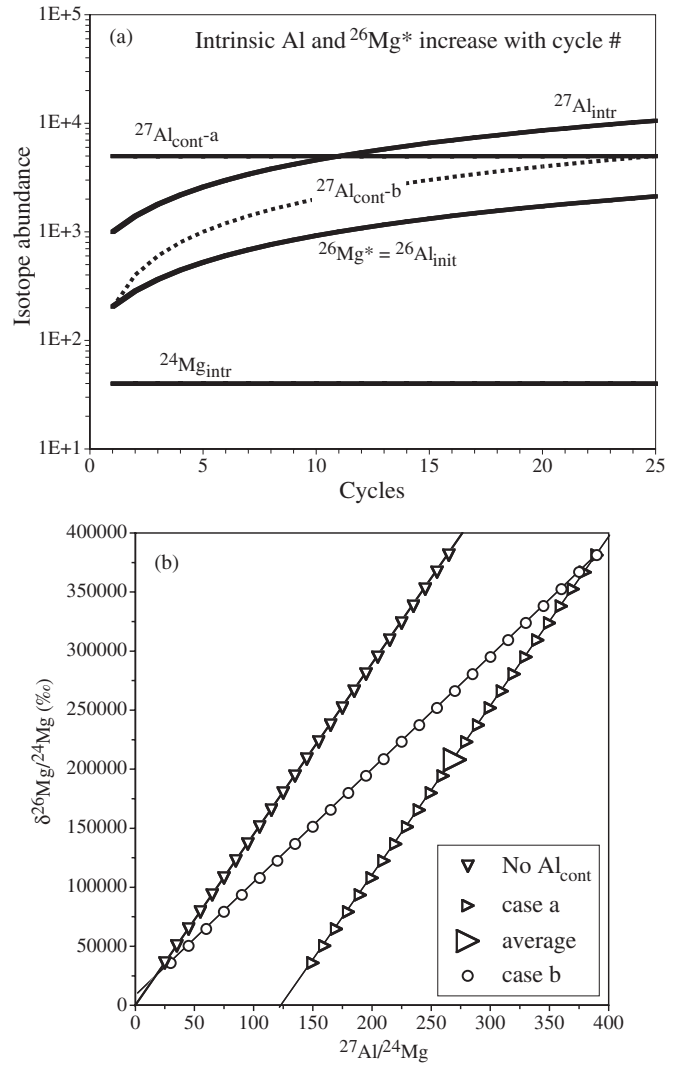


Figure 21. (a) Profiles of Al and Mg isotopes where the intrinsic Mg is constant and Al increases with cycle number. Also shown are assumed profiles of Al contamination, one assumed to be constant and the other to increase with cycle number. (b) Isotope correlation plot of $\delta^{26}\text{Mg}/^{24}\text{Mg}$ vs. $^{27}\text{Al}/^{24}\text{Mg}$ showing the result of the profiles in panel (a) with and without Al contamination.

assume that they both increase with cycle number and that intrinsic Mg is uniform (Figure 21(a)). This assumption also results in a wide range of $\delta^{26}\text{Mg}/^{24}\text{Mg}$ values and $^{27}\text{Al}/^{24}\text{Mg}$ ratios and a perfect correlation of the two (Figure 21 (b)). If we now add uniform Al, the data points shift to the right by the same distance (Figure 21(b)). We note that, in contrast to Figure 18(c), the slope of the correlation line does not change, because in this case Mg is constant. However, if we add Al contamination that increases with cycle number (Figures 21(a), case b), we obtain a straight correlation line with a smaller slope and a small positive intercept on the y-axis.

In summary, different combinations of intrinsic ^{27}Al and radiogenic ^{26}Mg with Mg and Al contamination result in a variety of “isochron” lines with different slopes, intercepts with the x- and y-axis. Only certain forms of contamination will give straight lines and among those only special cases will give lines reflecting the initial $^{26}\text{Al}/^{27}\text{Al}$ ratio. The same caveat holds for determination of the $^{26}\text{Al}/^{27}\text{Al}$ ratio from the average $\delta^{26}\text{Mg}/^{24}\text{Mg}$ versus $^{27}\text{Al}/^{24}\text{Mg}$ values. We discussed an example shown in Figure 19(b). An interesting example is provided by case a in Figure 21(b). Whereas the slope of the correlation

line reflects the correct $^{26}\text{Al}/^{27}\text{Al}$ ratio, a determination of this ratio from the average values is incorrect.

REFERENCES

- Amari, S., Anders, E., Virag, A., & Zinner, E. 1990, *Natur*, **345**, 238
 Amari, S., Lewis, R. S., & Anders, E. 1994, *GeCoA*, **58**, 459
 Amari, S., Lewis, R. S., & Anders, E. 1995, *GeCoA*, **59**, 1411
 Amari, S., Zinner, E., & Lewis, R. S. 1995, *ApJL*, **447**, L147
 Amari, S., Zinner, E., & Lewis, R. S. 1996, *ApJL*, **470**, L101
 Amari, S., Zinner, E., & Lewis, R. S. 1999, *ApJL*, **517**, L59
 Anders, E., & Grevesse, N. 1989, *GeCoA*, **53**, 197
 Bernatowicz, T. J., Amari, S., Zinner, E. K., & Lewis, R. S. 1991, *ApJL*, **373**, L73
 Bernatowicz, T. J., Cowsik, R., Gibbons, P. C., et al. 1996, *ApJ*, **472**, 760
 Besmehn, A., & Hoppe, P. 2003, *GeCoA*, **67**, 4693
 Clayton, D. D., & Nittler, L. R. 2004, *ARA&A*, **42**, 39
 Croat, T. K., Bernatowicz, T., Amari, S., Messenger, S., & Stadermann, F. J. 2003, *GeCoA*, **67**, 4705
 Croat, T. K., Stadermann, F. J., & Bernatowicz, T. J. 2005, *ApJ*, **631**, 976
 Croat, T. K., Stadermann, F. J., & Bernatowicz, T. J. 2008, *M&PS*, **43**, 1497
 Croat, T. K., Stadermann, F. J., & Bernatowicz, T. J. 2010, *AJ*, **139**, 2159
 Groopman, E., Wopenka, B., Bernatowicz, T. J., & Zinner, E. 2012, in *Lunar Planet. Sci. Conf. XLIII*, Abstract 2126
 Gyngard, F., Nittler, L. R., & Zinner, E. 2010, *M&PS*, **45**, A72
 Hinton, R. W. 1990, *ChGeo*, **83**, 11
 Hoppe, P., Amari, S., Zinner, E., & Lewis, R. S. 1995, *GeCoA*, **59**, 4029
 Hoppe, P., Fujiya, W., & Zinner, E. 2012, *ApJL*, **745**, L26
 Hoppe, P., Leitner, J., Gröner, E., et al. 2010, *ApJ*, **719**, 1370
 Hoppe, P., Stöckel, R., Eberhardt, P., Amari, S., & Lewis, R. S. 1996, *Sci*, **272**, 1314
 Hynes, K. M., & Gyngard, F. 2009, in *Lunar Planet. Sci. Conf. XL*, Abstract 1198
 Jadhav, M., Amari, S., Marhas, K. K., et al. 2008, *ApJ*, **682**, 1479
 Jadhav, M., Amari, S., Zinner, E., & Maruoka, T. 2006, *NewAR*, **50**, 591
 Jadhav, M., Amari, S., Zinner, E., et al. 2013, *GeCoA*, in press
 Limongi, M., & Chieffi, A. 2003, *ApJ*, **592**, 404
 Limongi, M., & Chieffi, A. 2006, *ApJ*, **647**, 483
 Lin, Y., Amari, S., & Pravdivtseva, O. 2002, *ApJ*, **575**, 257
 Lin, Y., Gyngard, F., & Zinner, E. 2010, *ApJ*, **709**, 1157
 Lodders, K. 2003, *ApJ*, **591**, 1220
 Lodders, K., & Amari, S. 2005, *ChEG*, **65**, 93
 Lugaro, M. 2005, *Stardust from Meteorites: An Introduction to Presolar Grains*, Vol. 9 (Singapore: World Scientific), 209
 Marhas, K. K., Amari, S., Gyngard, F., Zinner, E., & Gallino, R. 2008, *ApJ*, **689**, 622
 Meyer, B. S., Weaver, T. A., & Woosley, S. E. 1995, *Metic*, **30**, 325
 Nittler, L. R., Alexander, C. M. O. D., Gallino, R., et al. 2008, *ApJ*, **682**, 1450
 Nittler, L. R., Amari, S., Zinner, E., Woosley, S. E., & Lewis, R. S. 1996, *ApJL*, **462**, L31
 Rauscher, T., Heger, A., Hoffman, R. D., & Woosley, S. E. 2002, *ApJ*, **576**, 323
 Stadermann, F. J., Croat, T. K., Bernatowicz, T. J., et al. 2005, *GeCoA*, **69**, 177
 Timmes, F. X., Woosley, S. E., Hartmann, D. H., & Hoffman, R. D. 1996, *ApJ*, **464**, 332
 Travaglio, C., Gallino, R., Amari, S., et al. 1999, *ApJ*, **510**, 325
 Wasserburg, G. J., Gallino, R., Busso, M., Goswami, J. N., & Raiteri, C. M. 1995, *ApJL*, **440**, L101
 Woosley, S. E., & Weaver, T. A. 1995, *ApJS*, **101**, 181
 Wopenka, B., Groopman, E., & Zinner, E. 2011a, *M&PS*, **46**, A252
 Wopenka, B., Jadhav, M., & Zinner, E. 2011b, in *Lunar Planet. Sci. Conf. XLII*, Abstract 1162
 Wopenka, B., Xu, Y. C., Zinner, E., & Amari, S. 2013, *GeCoA*, **106**, 463
 Xu, X. C., Amari, S., Gyngard, F., Zinner, E., & Lin, Y. 2012, *M&PS*, **47**, 5104
 Zinner, E. 2007, in *Treatise on Geochemistry Update*, ed. H. D. Holland, K. K. Turekian, & A. Davis (Oxford: Elsevier), 1.02 (online update only), 1
 Zinner, E., Amari, S., & Jadhav, M. 2006, in *PoS(NIC-IX)019*
 Zinner, E., Gyngard, F., & Nittler, L. R. 2010a, in *Lunar Planet. Sci. Conf. XLI*, Abstract 1359
 Zinner, E., Jadhav, M., Gyngard, F., & Nittler, L. R. 2010b, *M&PS*, **45**, A225